

1 **A computational framework for time dependent**
2 **deformation in viscoelastic magmatic systems**

3 **Cody Rucker (crucker@uoregon.edu)¹, Brittany A. Erickson**
4 **(bae@uoregon.edu)^{1,2}, Leif Karlstrom (leif@uoregon.edu)², Brian Lee**
5 **(bl7@pdx.edu)³, and Jay Gopalakrishnan (gjay@pdx.edu)³**

6 ¹Department of Computer and Information Science, University of Oregon, Eugene, OR, USA

7 ²Department of Earth Sciences, University of Oregon, Eugene, OR, USA

8 ³Department of Mathematics and Statistics, Portland State University, Portland, OR, USA

9 This manuscript has been submitted for publication in the Journal of Geophys-
10 ical Research: Solid Earth. Please note that, despite having undergone peer-review, the
11 manuscript has yet to be formally accepted for publication. Subsequent versions of this
12 manuscript may have slightly different content. If accepted, the final version of this manuscript
13 will be available via the 'Peer-reviewed Publication DOI' link on the right-hand side of
14 this webpage. Please feel free to contact any of the authors; we welcome feedback.

Corresponding author: Cody Rucker, crucker@uoregon.edu

15

Key Points:

16

- A high-order numerical framework is derived for time-dependent viscoelastic deformation around magma reservoirs.

17

18

- Frequency domain transfer function characterizes phase lag and amplification between fields due to time-dependent rheology.

19

20

- The spatial extent of viscous response is frequency dependent and well-characterized by a local Deborah number.

21

Abstract

Time-dependent ground deformation is a key observable in active magmatic systems, but is challenging to characterize. Here we present a numerical framework for modeling transient deformation and stress around a subsurface, spheroidal pressurized magma reservoir within a viscoelastic half-space with variable material coefficients, utilizing a high-order finite-element method and explicit time-stepping. We derive numerically stable time steps and verify convergence. We then explore the frequency dependence of surface displacement associated with cyclic pressure applied to a spherical reservoir beneath a stress-free surface. We consider a Maxwell rheology and a steady geothermal gradient, which gives rise to spatially variable viscoelastic material properties. The temporal response of the system is characterized numerically with a transfer function that connects peak surface deformation amplitude and phase lag with respect to sinusoidal reservoir pressurization. Amplitude and phase of this transfer function vary with the frequency of pressure forcing. The volume of host rock exhibiting viscous response around the reservoir is also frequency dependent, depending on a threshold local Deborah number that measures the characteristic timescale for pressurization against a spatially varying Maxwell relaxation time. Although commonly idealized as a thin shell, we find that this dominantly viscous region may define a spatially complex brittle-ductile transition, depending on crustal thermal state, at longer forcing periods. Because arbitrary chamber pressure histories can be represented through a superposition of sinusoidal forcing, our results and general computational framework apply to a wide range of transient deformation scenarios relevant for characterizing transcrustal magmatic systems.

Plain Language Summary

Ground motions associated with subsurface magma reservoirs are the result both of magma movement and time-dependent deformation of crustal rocks. We have developed a new computational framework to help interpret surface deformations associated with magmatic systems embedded within viscoelastic rocks as expected in volcanic regions. This framework is general in the sense that a broad range of scientific studies can be explored by specifying particular conditions at domain boundaries or magma reservoir geometries, and we perform rigorous numerical tests to ensure credible solutions. We then apply the model to study a simple but highly generalizable type of transient behavior - the cyclic pressurization and depressurization of a spherical reservoir. We develop a theoretical approach to simply analyze the time-dependent output, and find that temporal lag and amplification of surface deformation with respect to the reservoir is explained by an aureole of material surrounding the chamber with a dominantly viscous

57 response, whose size is frequency-dependent. Our results can be extended to many tran-
58 sient deformation scenarios because a sinusoidal response forms the basic element of gen-
59 eral pressure time-series.

60 **1 Introduction**

61 Magma reservoirs represent a fundamental link between mantle melting and vol-
62 canic activity seen at the surface. Eruptions that drain these reservoirs are the most dra-
63 matic example of magma chamber mechanics, but a wide spectrum of time-varying sur-
64 face deformation and other unrest seen in volcanic regions likely has an origin within crustal
65 storage zones (Anderson & Segall, 2011; Cianetti et al., 2012; Henderson & Pritchard,
66 2017; Walwer et al., 2021). As a result, understanding controls on time-dependent magma
67 chamber deformation and stress is a long-standing research topic in volcanology (Sparks
68 et al., 2017; Segall, 2019). This is a challenging problem because time-dependence may
69 arise from magma reservoir magma evolution (mass balance, temperature changes, or
70 changes in magma compressibility due to volatile exsolution), or from mechanical response
71 of reservoir host rocks that are heated, damaged, and variably fluid-saturated. Alterna-
72 tively, transient forcing of magma reservoirs may be external in origin, for example from
73 tectonic activity or climate (Sigmundsson et al., 2010).

74 On sufficiently short time scales, it is appropriate to assume an elastic/brittle rhe-
75 ology of host rocks. Elastic models have been widely used to interpret geodetic data gath-
76 ered at volcanoes (Mogi, 1958; McTigue, 1987; Berrino et al., 1984). Such models pre-
77 dict that time-dependent behavior comes only from reservoir magma mass balance/state
78 variable changes (Cianetti et al., 2012) or boundary forcing, although poroelastic effects
79 can also lead to time-dependence (Mittal & Richards, 2019). Time dependent deforma-
80 tion and stress, especially for longer characteristic deformation rates of the reservoir (Liao
81 et al., 2021), likely involves ductile response of host rocks that behave in a viscoelastic
82 manner (Dragoni & Magnanensi, 1989).

83 Viscoelastic effects have been identified as defining a notion of magma chamber sta-
84 bility, providing a mechanism for relaxing stresses associated with build-up of overpres-
85 sure within the chamber. Viscoelastic effects may play a role in the development of large
86 silicic reservoirs (Jellinek & DePaolo, 2003) as well as eruption sequences from long-lived
87 magma reservoirs (Degruyter & Huber, 2014). They may help explain the magnitude
88 and time-dependence (Newman et al., 2001) of ground deformation at active volcanoes.
89 On longer timescales, state shifts in the magma transport system reflected by increas-
90 ing intrusive-extrusive ratios, and localization of volcanic output around spatial centers,
91 may also reflect time-evolving viscoelastic behavior (Karlstrom et al., 2015).

92 Viscoelastic effects are strongly tied to the thermal state of the magmatic system,
93 because rock rheology is temperature dependent. Thus it is to be expected that viscoelas-
94 tic response varies spatially, and evolves in time with the transcrustal magma transport
95 system. Such unsteady effects, both spatial and temporal, are poorly constrained. In-
96 stead it is typically assumed that magma reservoirs reside in a steady state geotherm (Del
97 Negro et al., 2009; Head et al., 2019), or that the mechanical response is well-approximated
98 by a pre-specified shell of viscous material in an elastic host (Bonafede et al., 1986; Segall,
99 2016). Time evolution is either imposed kinematically through stress boundary condi-
100 tions (e.g., to model an eruptive event, (Dragoni & Magnanensi, 1989)) or arises dynam-
101 ically through mass and energy balance (e.g., Karlstrom et al., 2010).

102 In this work, we present a robust numerical framework for simulating the thermo-
103 mechanical behavior of a subsurface magma reservoir in an isotropic, heterogeneous, vis-
104 coelastic halfspace subject to a periodic pressure variation at the chamber wall. This rep-
105 represents a different sort of idealization than previous studies: we consider the full com-
106 plexity of spatial variation in mechanical response, but treat time evolution as harmonic.
107 In this way we isolate the frequency dependence of the problem, and develop a trans-
108 fer function approach using analytic functions to predict material response. While we
109 anticipate that the sinusoidal forcing might approximate some natural magmatic evo-
110 lution (e.g., cyclic stress from seismic waves, eruption cycles, or glacial cycles), this ap-
111 proach also implies a superposition framework for studying much more general time evo-
112 lution.

113 Our model is developed to handle general axisymmetric geometries in the subsur-
114 face and surface, as well as lateral loads. However, we focus on the relatively simple and
115 well-studied case of a sphere in a half-space without remote loading to explore transient
116 effects, deriving material properties from a steady state temperature distribution within
117 the medium. After detailing the numerical framework we verify convergence using the
118 method of manufactured solutions (Roache, 1998). Finally we use the verified framework
119 to characterize the system’s response to spatially variable viscoelastic material proper-
120 ties. We develop a transfer function between chamber pressure and maximum vertical
121 surface deformation to demonstrate that two parameters – the phase lag between pres-
122 surization and surface deformation, and their relative amplitude – imply a frequency-
123 dependent viscoelastic response that depends on chamber temperature and geothermal
124 gradient magnitude. We also find that the spatial thermo-rheologic structure beneath
125 the chamber influences surface deformation at long forcing periods.

126 The paper is organized as follows. In Section 2 we introduce the governing equa-
127 tions and generic physical problem of interest. In Section 3 we discuss the computational

128 framework for solving our problem, stability considerations and resolution tests, and de-
 129 velop the specific non-dimensional time-dependent problem of interest. Section 4 intro-
 130 duces the transfer function approach that represents our primary analysis tool. Section
 131 5 then discusses results of computations and Section 6 discusses implications for mag-
 132 matic systems.

133 2 Mathematical Framework

134 2.1 Problem Formulation and Geometry

135 We consider a subsurface magma reservoir in an isotropic, viscoelastic half-space.
 136 In general the reservoir evolves in time in response to mass, momentum, and energy bal-
 137 ance associated with magma transport. We focus here on the host response to bulk state
 138 variable changes within the reservoir, parameterized as uniform but time-evolving pres-
 139 sure on the reservoir wall.

140 We employ a cylindrical coordinate system (r, z, θ) with the origin at the reservoir
 141 center. The assumption of axisymmetry means the problem shows no variation along the
 142 θ -coordinate enabling solutions in the one-sided (r, z) -plane. Figure 1 illustrates the
 143 geometry which defines the computational region surrounding a reservoir. The magma
 144 cavity has horizontal axis $a > 0$ and vertical axis $b > 0$, with center at the origin, and
 145 Earth's free surface at $z = D + b$ (z positive upwards). Maximum depth of the com-
 146 putational domain is denoted by L_z and the maximum lateral distance from the center
 147 of radial symmetry is denoted by L_r .

148 We construct the region outside of the cavity by intersecting a closed, rectangu-
 149 lar region $\mathcal{D} = \{(r, z) \in \mathbb{R}^2 \mid 0 < r < L_r, -L_z < z < D + b\}$ and a punctured do-
 150 main $\mathcal{B} = \{(r, z) \in \mathbb{R}^2 \mid \frac{r^2}{a^2} + \frac{z^2}{b^2} > 1\}$. The region Ω outside of the cavity, defined
 151 by $\Omega = \mathcal{D} \cap \mathcal{B}$ forms our two-dimensional computational domain. The physical three-
 152 dimensional problem is posed on the revolution of Ω , the three-dimensional domain we
 153 denote by $\check{\Omega}$.

154 2.2 Governing Equations

155 We assume sufficiently slow deformation so that quasi-static viscoelasticity is a valid
 156 description of the momentum balance. We assume the medium is a Maxwell material.
 157 Let $\mathbf{u}, \underline{\underline{\epsilon}}, \underline{\underline{\gamma}}, \underline{\underline{\sigma}}$ be, respectively, the displacement vector, the total strain tensor, the vis-
 158 cous strain tensor, and the stress tensor. The time derivative of $\underline{\underline{\gamma}}$ is denoted by $\dot{\underline{\underline{\gamma}}}$. The

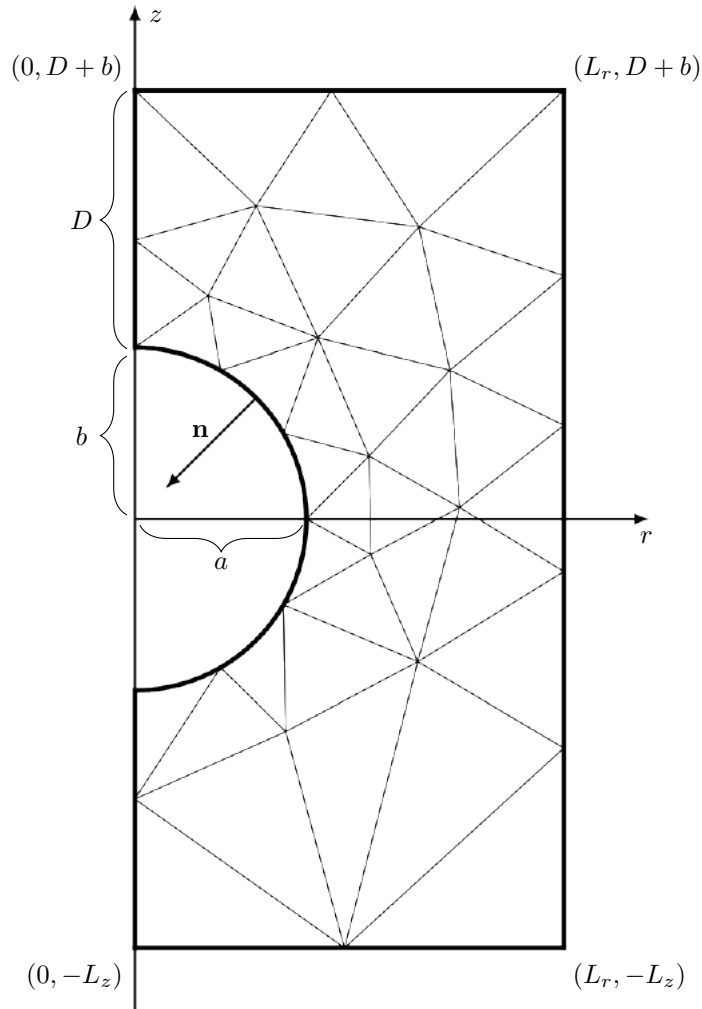


Figure 1. The region outside a subsurface, spheroidal magma reservoir centered at the origin. The reservoir has a horizontal axis $a > 0$ and vertical axis $b > 0$. The distance from the top of the reservoir to the surface is $D > b$. The region is bounded by a maximal depth L_z and maximal distance from the radial center L_r .

159 relevant governing equations are:

$$160 \quad \operatorname{div} \underline{\boldsymbol{\sigma}} = \mathbf{f} \quad \text{in } \check{\check{\Omega}}, \quad (1a)$$

$$161 \quad \dot{\underline{\boldsymbol{\gamma}}} = \mathbf{A} \underline{\boldsymbol{\sigma}} \quad \text{in } \check{\check{\Omega}}, \quad (1b)$$

$$162 \quad \underline{\boldsymbol{\sigma}} = \mathbf{E}(\underline{\boldsymbol{\varepsilon}}(\mathbf{u}) - \underline{\boldsymbol{\gamma}}) \quad \text{in } \check{\check{\Omega}}, \quad (1c)$$

163 where $\underline{\boldsymbol{\varepsilon}}(\mathbf{u}) = (\nabla \mathbf{u} + \nabla \mathbf{u}^T)/2$, \mathbf{E} is the fourth-order, isotropic elastic stiffness tensor
 164 whose (i, j, k, l) -component in Cartesian coordinates is given by

$$165 \quad E_{ijkl} = \lambda \delta_{ij} \delta_{kl} + \mu (\delta_{ik} \delta_{jl} + \delta_{il} \delta_{jk}). \quad (2)$$

166 Here, μ denotes the shear modulus, λ denotes Lamé's first parameter, and δ denotes the
 167 components of the identity tensor. The fourth-order tensor \mathbf{A} relates viscous strain to
 168 stress, and is derived from the Maxwell constitutive law (Muki & Sternberg, 1961) to pro-
 169 duce the form

$$170 \quad \mathbf{A} \underline{\boldsymbol{\sigma}} = \frac{1}{2\eta} \left(\sigma_{ij} - \frac{1}{3} \sigma_{kk} \delta_{ij} \right), \quad (3)$$

171 where η denotes the viscosity. Equation (1a) is the static equilibrium equation where \mathbf{f}
 172 represents body forces. Equation (1b) is the aging law for a Maxwell material and Equa-
 173 tion (1c) is Hooke's Law. When supplemented by initial and boundary conditions, the
 174 system (1a) can be solved in any coordinate system.

175 We proceed to use the cylindrical coordinate system (r, z, θ) to exploit axial sym-
 176 metry. Accordingly, we write the displacement vector field as $\mathbf{u} = u_r \mathbf{e}_r + u_z \mathbf{e}_z + u_\theta \mathbf{e}_\theta$
 177 where \mathbf{e}_r , \mathbf{e}_θ , and \mathbf{e}_z denote the unit vectors of the cylindrical coordinate system. The
 178 source \mathbf{f} can also be similarly expressed. We assume that u_θ and f_θ are zero. Further-
 179 more, by the assumption of axial symmetry, u_r and u_z are independent of the azimuthal
 180 variable θ , i.e., their partial derivatives $\partial_\theta u_i$ vanish for all $i \in \{r, z\}$. Hence, employ-
 181 ing the cylindrical components of the strain tensor, displacements in the Earth are re-
 182 lated to strains by

$$183 \quad \underline{\boldsymbol{\varepsilon}}(\mathbf{u}) = \frac{u_r}{r} \mathbf{e}_\theta \otimes \mathbf{e}_\theta + \sum_{i,j \in \{r,z\}} \frac{1}{2} (\partial_i u_j + \partial_j u_i) \mathbf{e}_i \otimes \mathbf{e}_j. \quad (4)$$

184 The stress tensor, which takes the same form as above, can be expressed, omitting its
 185 zero components, as follows:

$$186 \quad \underline{\boldsymbol{\sigma}} = \sigma_{\theta\theta} \mathbf{e}_\theta \otimes \mathbf{e}_\theta + \sum_{i,j \in \{r,z\}} \sigma_{ij} \mathbf{e}_i \otimes \mathbf{e}_j. \quad (5)$$

187 Using the formula for the divergence of a tensor in cylindrical coordinates, the equilib-
 188 rium equation (1a) then takes the form

$$189 \quad \left(\partial_r \sigma_{rr} + \partial_z \sigma_{rz} + \frac{1}{r} (\sigma_{rr} - \sigma_{\theta\theta}) \right) \mathbf{e}_r + \left(\partial_r \sigma_{rz} + \partial_z \sigma_{zz} + \frac{1}{r} \sigma_{rz} \right) \mathbf{e}_z = \mathbf{f}. \quad (6)$$

190 Using (4) and (1c) to obtain expressions for the cylindrical components of the stress ten-
 191 sor, the equilibrium equation (6) can be solved for the components of the displacement
 192 in the two-dimensional meridian (rz) plane. This reduction from three to two dimen-
 193 sions provides substantial computational efficiency.

194 To reduce the problem to the meridian half-plane where $r > 0$, we need to im-
 195 pose the following boundary conditions on the axial boundary $\Gamma_0 = \{(r, z) \in \partial\Omega : r = 0\}$, namely

$$197 \quad u_r = 0, \quad \text{on } \Gamma_0 \quad (7a)$$

$$198 \quad \sigma_{rz} = 0, \quad \text{on } \Gamma_0. \quad (7b)$$

199 The first follows from a “no-opening” condition at $r = 0$. To see the second, consider
 200 the three-dimensional vector field $\mathcal{T} = \underline{\sigma} \cdot \mathbf{e}_z$ (where the dot notation between a sec-
 201 ond and first order tensor signifies $\mathcal{T}_i = \underline{\sigma}_{ij}e_{z_j}$, repeated indices indicate summation
 202 over that index) on a plane orthogonal to the $r = 0$ axis whose unit normal vector is
 203 \mathbf{e}_z . The continuity of this force field at $r = 0$ requires that (7b) holds. Other bound-
 204 ary conditions are imposed by partitioning the remaining boundary $\partial\Omega \setminus \Gamma_0$. We let $\Gamma_{\text{disp}} \subseteq$
 205 $\partial\Omega$ and $\Gamma_{\text{trac}} = \partial\Omega \setminus \Gamma_{\text{disp}}$ denote a general partitioning of $\partial\Omega$ into subdomains where
 206 either displacement or traction boundary conditions are imposed, respectively. Explic-
 207 itly, these conditions are

$$208 \quad \mathbf{u} = \mathbf{g}_{\text{disp}}(t) \quad \text{on } \Gamma_{\text{disp}}, \quad (7c)$$

$$209 \quad \underline{\sigma} \cdot \mathbf{n} = \mathbf{g}_{\text{trac}}(t) \quad \text{on } \Gamma_{\text{trac}}, \quad (7d)$$

210 where \mathbf{n} is the outward unit normal to the domain Ω , and $\mathbf{g}_{\text{disp}}, \mathbf{g}_{\text{trac}}(t)$ are given, time-
 211 varying boundary data. This general model enables the study of reservoir pressure, lat-
 212 eral loads and topography, among other studies in axisymmetric geometries.

213 In addition to boundary conditions, we must also supplement the aging law, Equa-
 214 tion (1b), with an initial condition on viscous strain, namely

$$215 \quad \underline{\gamma}(r, z, t = 0) = \underline{\gamma}_0(r, z), \quad (r, z) \in \Omega. \quad (8)$$

216 **3 Computational Framework**

217 We solve initial-boundary-value problem (Equations (1a),(4)-(8)) numerically by
 218 pairing a finite difference discretization in time with a finite element method (FEM) in
 219 space. As described in this section, at each time step the spatial problem is governed by
 220 static equilibrium, with viscous effects manifested as a time-dependent source term. Sim-
 221 ulations are done using Python code developed on top of the free and open source multi-
 222 physics library NGSolve (Schöberl, 2010–2022) and the accompanying mesh generator (Schöberl,

1997). The Python code is available in a public repository (*Bitbucket: magmaxisym*, 2022).
 Curved elements are used to obtain good geometrical conformity with the magma cavity boundary. The following subsections outline the static problem, the temporal discretization, and the details of the specific problem considered in this work.

3.1 Solving the Static Equilibrium Equation

We solve the equilibrium equations (1a) subject to boundary conditions (7) using a FEM, which requires the weak form of the problem. To construct the weak form, we perform the following steps: (i) multiply equation (6) by r and take the dot product of both sides with a test function $\mathbf{v} = v_r \mathbf{e}_r + v_z \mathbf{e}_z$, (ii) integrate by parts on Ω , (iii) replace σ_{ij} by functions of u_i using (4) and (1c), and (iv) incorporate the boundary conditions of (7), letting \mathbf{v} take on homogeneous displacement boundary conditions on Γ_{disp} . The result is the equation

$$\int_{\Omega} \mathbf{E}(\underline{\boldsymbol{\varepsilon}}(\mathbf{u}) - \underline{\boldsymbol{\gamma}}) : \underline{\boldsymbol{\varepsilon}}(\mathbf{v}) r dr dz - \int_{\Gamma_{\text{trac}}} \mathbf{g}_{\text{trac}} \cdot \mathbf{v} r ds = - \int_{\Omega} \mathbf{f} \cdot \mathbf{v} r dr dz. \quad (9)$$

Here the colon denotes the Frobenius inner product. To simplify notation, we let $(\cdot, \cdot)_r$ and $\langle \cdot, \cdot \rangle_r$ respectively denote the integrals over Ω and Γ_{trac} of r multiplied by the appropriate (dot or Frobenius) inner product of the arguments. Then the above equation may be rewritten as

$$(\mathbf{E}\underline{\boldsymbol{\varepsilon}}(\mathbf{u}), \underline{\boldsymbol{\varepsilon}}(\mathbf{v}))_r = -(\mathbf{f}, \mathbf{v})_r + \langle \mathbf{g}_{\text{trac}}, \mathbf{v} \rangle_r + (\mathbf{E}\boldsymbol{\gamma}, \mathbf{v})_r. \quad (10)$$

The Lagrange FEM is derived by imposing the above equation on a space of piecewise polynomials. Given a triangulation of Ω , denoted by Ω_h , the Lagrange finite element space of order p , denoted by V_h consists of all functions which are continuous on Ω whose restriction to each element K of Ω_h is a polynomial of degree at most p in r and z . In the FEM, the data \mathbf{f} and \mathbf{g}_{trac} are integrated while the data \mathbf{g}_{disp} is interpolated. Assuming the latter interpolation is done, let

$$\mathbf{V}_h^{\mathbf{g}_{\text{disp}}} = \{\mathbf{v} = v_r \mathbf{e}_r + v_z \mathbf{e}_z : v_r \in V_h, v_z \in V_h, \text{ and } \mathbf{v}|_{\Gamma_{\text{disp}}} = \mathbf{g}_{\text{disp}}\}.$$

Also let

$$\mathbf{V}_h^0 = \{\mathbf{v} = v_r \mathbf{e}_r + v_z \mathbf{e}_z : v_r \in V_h, v_z \in V_h, \text{ and } \mathbf{v}|_{\Gamma_{\text{disp}}} = \mathbf{0}\}.$$

Then, the FEM computes $\mathbf{u}_h \in \mathbf{V}_h^{\mathbf{g}_{\text{disp}}}$ satisfying

$$(\mathbf{E}\underline{\boldsymbol{\varepsilon}}(\mathbf{u}_h), \underline{\boldsymbol{\varepsilon}}(\mathbf{v}))_r = -(\mathbf{f}, \mathbf{v})_r + \langle \mathbf{g}_{\text{trac}}, \mathbf{v} \rangle_r + (\mathbf{E}\boldsymbol{\gamma}, \mathbf{v})_r, \quad \text{for all } \mathbf{v} \in \mathbf{V}_h^0, \quad (11)$$

provided \mathbf{f} , \mathbf{g}_{disp} , \mathbf{g}_{trac} , and $\boldsymbol{\gamma}$ are given. Equation (11) leads to a linear system of equations once a finite element basis of shape functions is used.

254

3.2 Temporal Discretization

255

256

257

258

259

Our time-stepping method is inspired by that of Allison and Dunham (2018) where viscous strains appear as a time-dependent source term on the equilibrium equation. As can be seen from Equation (11), once γ is known at any given time, using it as source, a displacement approximation can be computed by solving (11). However, to compute γ , we need to apply a time integrator to the aging law, Equation (1b).

260

261

262

263

To this end, for computational purposes only it is convenient to let $\underline{\mathbf{C}} = \mathbf{E}\underline{\boldsymbol{\gamma}}$, since the use of $\underline{\mathbf{C}}$ allows us to skip the assembly and inversion of a mass matrix made of inhomogeneous material coefficients. Since \mathbf{E} is time independent, simplifying $\mathbf{E}\mathbf{A}\underline{\boldsymbol{\sigma}} = (\mu/\eta)\text{dev}(\underline{\boldsymbol{\sigma}})$, Equation (1b) implies

264

$$\dot{\underline{\mathbf{C}}} = \frac{\mu}{\eta} \text{dev} \underline{\boldsymbol{\sigma}}. \quad (12)$$

265

266

267

268

269

270

271

Here $\text{dev}(\underline{\boldsymbol{\sigma}})$ denotes deviatoric tensor $\underline{\boldsymbol{\sigma}} - \text{tr}(\underline{\boldsymbol{\sigma}})$. Time integration of Equation (12) is carried out using the first-order accurate forward Euler method (chosen for its simplicity as we lay the computational groundwork; higher order methods will be incorporated in future developments). At each time step, we solve the weak form of equilibrium equation (Equation (11)) and use the computed displacement to obtain approximate $\underline{\mathbf{C}}$ at the next time step. To illustrate time-stepping explicitly, assume all fields are known at time t^n . The procedure to integrate to t^{n+1} over step size $\Delta t = t^{n+1} - t^n$ is as follows:

272

1. Use \mathbf{u}_h^n to update $\underline{\mathbf{C}}$ via forward Euler

273

$$\underline{\mathbf{C}}^{n+1} = \underline{\mathbf{C}}^n + \Delta t \frac{\mu}{\eta} \text{dev}(\mathbf{E}\underline{\boldsymbol{\varepsilon}}(\mathbf{u}_h^n) - \underline{\mathbf{C}}^n). \quad (13)$$

274

275

276

2. Compute data \mathbf{f}^{n+1} , $\mathbf{g}_{\text{disp}}^{n+1}$, $\mathbf{g}_{\text{trac}}^{n+1}$ at time t^{n+1} and use them, together with the output of the previous step, to solve the static equation: compute $\mathbf{u}_h^{n+1} \in \mathbf{V}_h^{\mathbf{g}_{\text{disp}}^{n+1}}$ satisfying

277

$$(\mathbf{E}\underline{\boldsymbol{\varepsilon}}(\mathbf{u}_h^{n+1}), \underline{\boldsymbol{\varepsilon}}(\mathbf{v}))_r = -(\mathbf{f}^{n+1}, \mathbf{v})_r + \langle \mathbf{g}_{\text{trac}}^{n+1}, \mathbf{v} \rangle_r + (\underline{\mathbf{C}}^{n+1}, \mathbf{v})_r \quad (14)$$

278

for all $\mathbf{v} \in \mathbf{V}_h^0$.

279

3.3 Model Specifics and Non-Dimensionalization

280

281

282

283

284

285

The majority of analysis in this work will examine how a realistic distribution of viscoelastic properties impacts deformation around magma reservoirs subject to cyclic loading. We proceed by idealizing the boundary pressure as a sinusoid, which approximates a canonical problem in viscoelasticity (Golden & Graham, 1988), and provides a framework for studying arbitrary time dependent signals through superposition. We thus assume a specific boundary partition where Γ_{trac} encompasses the reservoir wall,

286 Earth's free surface, and the computational boundary at depth ($z = -L_z$). Γ_{disp} is the
 287 lateral boundary $r = L_r$. We then set specific boundary data

$$288 \quad \mathbf{g}_{\text{disp}}(t) = 0, \quad (15)$$

289 so that displacements vanish at $r = L_r$. At Earth's free surface and at depth we take

$$290 \quad \mathbf{g}_{\text{trac}}(t) = 0. \quad (16)$$

291 At the reservoir wall we set

$$292 \quad -\mathbf{n} \cdot \mathbf{g}_{\text{trac}}(t) = P(t), \quad (17a)$$

$$293 \quad \mathbf{m} \cdot \mathbf{g}_{\text{trac}}(t) = 0, \quad (17b)$$

294 where

$$295 \quad P(t) = P_0 \sin(\omega t). \quad (18)$$

296 Equation 17a sets the normal component of the traction vector (the pressure) equal to
 297 a sinusoidal time-varying condition with amplitude P_0 and frequency ω . In what follows
 298 we will often refer to forcing period

$$299 \quad \tau = 2\pi/\omega \quad (19)$$

300 rather than frequency. Equation 17b imposes that the shear component of traction be
 301 equal to 0, where vector $\mathbf{m} = \mathbf{n} \times \mathbf{e}_z$ is tangent to the reservoir wall.

302 Non-dimensionalization of the governing equations reveals important physical pa-
 303 rameters and re-scales the problem to help reduce round-off errors. We begin by han-
 304 dling the scaling of the spatial domain before addressing governing equations. Tildes in
 305 what follows indicate non-dimensional variables. Let $r = a\tilde{r}$, $z = a\tilde{z}$, $\tilde{\mathcal{D}} = \{(\tilde{r}, \tilde{z}) \in$
 306 $\mathbb{R}^2 \mid 0 \leq \tilde{r} \leq \frac{L_r}{a}, -\frac{L_z}{a} \leq \tilde{z} \leq \frac{D+b}{a}\}$ and $\tilde{\mathcal{B}} = \{(\tilde{r}, \tilde{z}) \in \mathbb{R}^2 \mid \tilde{r}^2 + \frac{a^2}{b^2}\tilde{z} \geq 1\}$. Then our
 307 resulting scaled domain is given by

$$308 \quad \tilde{\Omega} = \tilde{\mathcal{D}} \cap \tilde{\mathcal{B}}, \quad (20)$$

309 with scaled boundaries $\tilde{\Gamma}_{\text{disp}}$ still representing the (scaled) lateral boundary and $\tilde{\Gamma}_{\text{trac}}$
 310 the (scaled) reservoir wall, Earth's free surface, and computational boundary at depth.
 311 We also scale displacements by a , namely $a\tilde{\mathbf{u}} = \mathbf{u}$, which effectively means that total
 312 strain $\underline{\epsilon}$ is not scaled. We scale stress, \mathbf{E} and time by the amplitude and frequency of
 313 the sinusoidal pressure, and body force by its magnitude F_0 (for example magnitude of
 314 gravitational force), giving

$$315 \quad \underline{\sigma} = P_0 \tilde{\underline{\sigma}}, \quad (21)$$

$$316 \quad \mathbf{E} = P_0 \tilde{\mathbf{E}}, \quad (22)$$

$$317 \quad \mathbf{f} = F_0 \tilde{\mathbf{f}}, \quad (23)$$

$$318 \quad t\omega = \tilde{t}, \quad (24)$$

319 which implies a scaling of $\underline{\mathbf{C}} = P_0 \tilde{\underline{\mathbf{C}}}$. The scaled form of the equilibrium equation (1a)
 320 is thus

$$321 \quad \text{div } \tilde{\underline{\boldsymbol{\sigma}}} = \frac{aF_0}{P_0} \tilde{\underline{\mathbf{f}}}, \quad (25)$$

322 and Hooke's law Equation (1c) becomes

$$323 \quad \tilde{\underline{\boldsymbol{\sigma}}} = \frac{\underline{\mathbf{E}}}{P_0} (\underline{\boldsymbol{\varepsilon}} - \underline{\boldsymbol{\gamma}}). \quad (26)$$

324 The two dimensionless parameters in Equations 25-26 physically represent the ratio of
 325 body force to reservoir boundary tractions, and a scaled reservoir pressure, respectively.

326 The modified aging law (Equation (12)) becomes

$$327 \quad \partial_{\tilde{t}} \tilde{\underline{\mathbf{C}}} = \frac{1}{De} \text{dev } \tilde{\underline{\boldsymbol{\sigma}}}, \quad (27)$$

328 where

$$329 \quad De = \frac{\eta\omega}{\mu} = \frac{2\pi\eta}{\tau\mu} \quad (28)$$

330 is the non-dimensional Deborah number. This ratio of elastic pressurization to viscous
 331 relaxation timescales commonly appears as a control parameter in models for magma
 332 chamber mechanics (Jellinek & DePaolo, 2003), cycles of eruptions (Degruyter & Hu-
 333 ber, 2014; Black & Manga, 2017), and the spatial structure of transcrystal magma sys-
 334 tems (Karlstrom et al., 2017; Huber et al., 2019). It will play an important role in our
 335 results.

336 Computationally, all problems considered in this work are solved in this non-dimensional
 337 form. The specific non-dimensional boundary conditions we thus take are

$$338 \quad \tilde{\underline{\mathbf{u}}} = 0 \quad \text{on } \tilde{\Gamma}_{\text{disp}}, \quad (29a)$$

$$339 \quad \tilde{\underline{\boldsymbol{\sigma}}}\mathbf{n} = \tilde{\underline{\mathbf{g}}}_{\text{trac}}(\tilde{t}) \quad \text{on } \tilde{\Gamma}_{\text{trac}}, \quad (29b)$$

340 and at the reservoir wall,

$$341 \quad -\mathbf{n} \cdot \tilde{\underline{\mathbf{g}}}_{\text{disp}}(\tilde{t}) = \tilde{P}(\tilde{t}) \quad (30)$$

$$342 \quad \mathbf{m} \cdot \tilde{\underline{\mathbf{g}}}_{\text{trac}}(\tilde{t}) = 0. \quad (31)$$

343 where $\tilde{P}(\tilde{t}) = \sin(\tilde{t})$. For all our applications we assume negligible body forces, so $aF_0/P_0 \ll$
 344 1.

345 **3.4 Stability and Verification**

346 Owing to the use of an explicit time-stepping scheme, it is necessary to establish
 347 conditions for which the scheme outlined in the previous section is stable. As an initial
 348 calculation, note that

$$349 \quad \underline{\mathbf{E}}\underline{\mathbf{A}}\underline{\boldsymbol{\sigma}} = \frac{\mu}{\eta} \text{dev } \underline{\boldsymbol{\sigma}}. \quad (32)$$

350 The deviatoric operator in Equation (32) can be expressed as a matrix-vector multipli-
 351 cation, namely

$$352 \quad \mathbf{E}\mathbf{A}\underline{\boldsymbol{\sigma}} = \frac{\mu}{\eta}\mathcal{D}\underline{\boldsymbol{\sigma}}, \quad (33)$$

353 if second-order tensors are stacked into vectors (across rows and removing symmetries)

$$354 \quad \underline{\boldsymbol{\sigma}} = [\sigma_{rr}, \sigma_{rz}, \sigma_{zz}, \sigma_{\theta\theta}]^T, \quad (34)$$

355 and matrix \mathcal{D} is given by

$$356 \quad \mathcal{D} = \begin{bmatrix} \frac{2}{3} & -\frac{1}{3} & -\frac{1}{3} & 0 \\ -\frac{1}{3} & \frac{2}{3} & -\frac{1}{3} & 0 \\ -\frac{1}{3} & -\frac{1}{3} & \frac{2}{3} & 0 \\ 0 & 0 & 0 & 1 \end{bmatrix}. \quad (35)$$

357 The non-dimensionalized explicit forward-Euler discretization of the aging law (Equa-
 358 tion (27)) can therefore be expressed as

$$359 \quad \underline{\tilde{\mathbf{C}}}^{n+1} = (\mathbf{I} - \Delta\tilde{t}De^{-1}\mathcal{D})\underline{\tilde{\mathbf{C}}}^n + \Delta\tilde{t}De^{-1}\mathcal{D}\underline{\tilde{\mathbf{E}}}\underline{\boldsymbol{\varepsilon}}^n, \quad (36)$$

360 the stability of which is determined by the eigenvalues of the growth-factor matrix $\mathbf{I} -$
 361 $\Delta\tilde{t}De^{-1}\mathcal{D}$ and whether we can bound its spectral radius using an appropriate choice for
 362 $\Delta\tilde{t}$. Eigenvalues for the growth-factor matrix are

$$363 \quad \lambda_1 = 1, \quad (37a)$$

$$364 \quad \lambda_2 = 1 - \frac{2}{3}\Delta\tilde{t}De^{-1}, \quad (37b)$$

$$365 \quad \lambda_3 = 1 - \Delta\tilde{t}De^{-1}, \quad (37c)$$

366 where λ_3 appears as a repeated eigenvalue. To bound their magnitudes by at most 1 de-
 367 mands that $\Delta\tilde{t}$ be smaller than $2De$. In addition, the time step must be sufficiently small
 368 to resolve any time-varying boundary data. In this work this amounts to resolving the
 369 sinusoidal boundary data at the reservoir wall. Since the corresponding (angular) Nyquist
 370 frequency for $\sin(\tilde{t})$ is 1, the largest time step that resolves this frequency is $\delta\tilde{t} = \pi$, and
 371 should be (in practice) a small fraction of this. A sufficient, stable time step is then cho-
 372 sen by

$$373 \quad \Delta\tilde{t} \leq \min\{2De, \delta\tilde{t}\}. \quad (38)$$

374 In practice we use more restrictive criteria, namely,

$$375 \quad \Delta\tilde{t} \leq \min\left\{\frac{De}{4}, \frac{\delta\tilde{t}}{2}\right\}. \quad (39)$$

376 Except for a few limiting cases, the temperature-dependent material parameters will cause
 377 $\frac{De}{4}$ to be the agent that restricts time-step. Our numerical method is verified for cor-
 378 rectness via rigorous convergence tests in both space and time via the method of man-
 379 ufactured solutions (Roache, 1998), with details provided in Appendix A.

380

3.5 Temperature-Dependent Material Parameters

381

382

383

384

385

386

387

We assume that viscosity of crustal rocks is described by a temperature-dependent Arrhenius relation. This neglects grain-size and stress-dependent effects (Bürgmann & Dresen, 2008), but parameterizes our assumption that temperature is the dominant factor controlling crustal rheology during crustal magma transport. In general, temperature evolves in time in response to magmatism (e.g., Karakas et al., 2017), but we assume a steady state geotherm here as our goal is simply to explore the role of realistic spatial structure of material parameters.

388

Accordingly, we solve the stationary heat equation

389

$$\nabla^2 T = 0 \quad \text{in } \check{\Omega}, \quad (40)$$

390

391

392

where $T(r, z)$ is the temperature field, which we assume to be axisymmetric. At the top, bottom and lateral parts of the boundary, we enforce a steady-state geothermal profile given by

393

$$T(z) = T_s - \alpha(z - (D + b)), \quad (41)$$

394

395

396

397

398

399

400

401

where T_s is the surface temperature constant and α is a parameter specifying the temperature gradient. At the chamber wall we set $T = T_c$, a constant temperature. We use a standard finite element formulation with radial weighting to reduce the problem to the two-dimensional domain Ω and as usual—see e.g., Gopalakrishnan and Pasciak (2006)—set zero temperature flux $\nabla T = 0$ at Γ_0 , the $r = 0$ boundary, to maintain our consideration of a one-sided problem. The solution of this BVP for the heat equation informs the temperature field throughout the domain, from which the viscosity is deduced according to the Arrhenius formula

402

$$\eta = A_D \exp\left(\frac{E_a}{RT}\right) \quad (42)$$

403

404

where A_D is the Dorn parameter, E_a is the activation energy, and R is the Boltzmann constant. For numerical computation, we prefer to use the equivalent formula

405

$$\eta = \eta_0 \exp\left(\frac{E_a}{R} \left[\frac{1}{T} - \frac{1}{T_s}\right]\right), \quad (43)$$

406

407

where $\eta_0 = A_D \exp\left(\frac{E_a}{RT_s}\right)$, to avoid numerical issues associated with very large viscosities predicted by low temperatures in the near surface.

408

409

410

411

Because numerically stable time steps depend on Deborah number (i.e. Equation 38) in our approach, the exponential dependence of viscosity leads to prohibitively small time steps at high temperatures. This limits the degree to which we can exactly explore temperatures appropriate for more mafic magmas in this work.

Elastic parameters are also considered to be temperature dependent. Bakker et al. (2016) provide smooth and continuous forms for temperature-dependent Young's modulus $E(T)$ and Poisson's ratio $\nu(T)$ as

$$E(T) = c_1 \left[1 - \operatorname{erf} \left(\frac{T - \bar{T}}{s} \right) \right] + c_2 T + c_3, \quad (44)$$

$$\nu(T) = \left[1 - \frac{E}{E_{\max}} \right] \cdot [\nu_{\max} - \nu_{\min}] + \nu_{\min} \quad (45)$$

where $\nu_{\min} = 0.25$, $\nu_{\max} = 0.49$ define the range of possible Poisson's ratios and E_{\max} is the max value Young's modulus achieves for a given temperature profile. \bar{T} is a temperature threshold for which Young's modulus decreases by an order of magnitude and c_1, c_2, c_3, s are empirical parameters. To convert E and ν to λ, μ (the proper elastic moduli for our framework), we use $\lambda = \frac{E\nu}{(1+\nu)(1-2\nu)}$, $\mu = \frac{E}{2(1+\nu)}$. Figure 2 demonstrates the spatial pattern exhibited by the material parameters for a temperature profile characterized by 800°C reservoir temperature, 0°C surface temperature and a geothermal gradient of 20°C/km.

4 Framework for Time-Dependent Analysis

We now develop tools to analyze the time evolution of viscoelastic deformation predicted from our numerical calculations. Towards our goal of examining how a realistic distribution of viscoelastic properties impacts deformation around magma reservoirs subject to cyclic loading, we begin with a 1D analysis to illustrate inherent properties of the system which may be generalized in the 2D problem.

4.1 Insights from the 1D Maxwell Model

Given the spatial domain $x \in [0, L]$, the 1D strain-displacement relation is given by

$$\varepsilon = u_x \quad (46)$$

and the 1D governing equations (equilibrium, viscous strain evolution and Hooke's law, respectively) are

$$\frac{\partial \sigma}{\partial x} = 0, \quad (47a)$$

$$\dot{\gamma} = \frac{1}{\eta} \sigma, \quad (47b)$$

$$\sigma = \mu(\varepsilon - \gamma), \quad (47c)$$

where σ , ε , γ , and u are, respectively, the 1D stress, total strain, viscous strain, and displacement. Boundary conditions are chosen to reflect the conditions for the 2D problem. The origin experiences the sinusoidal pressure condition (representing the reservoir) and

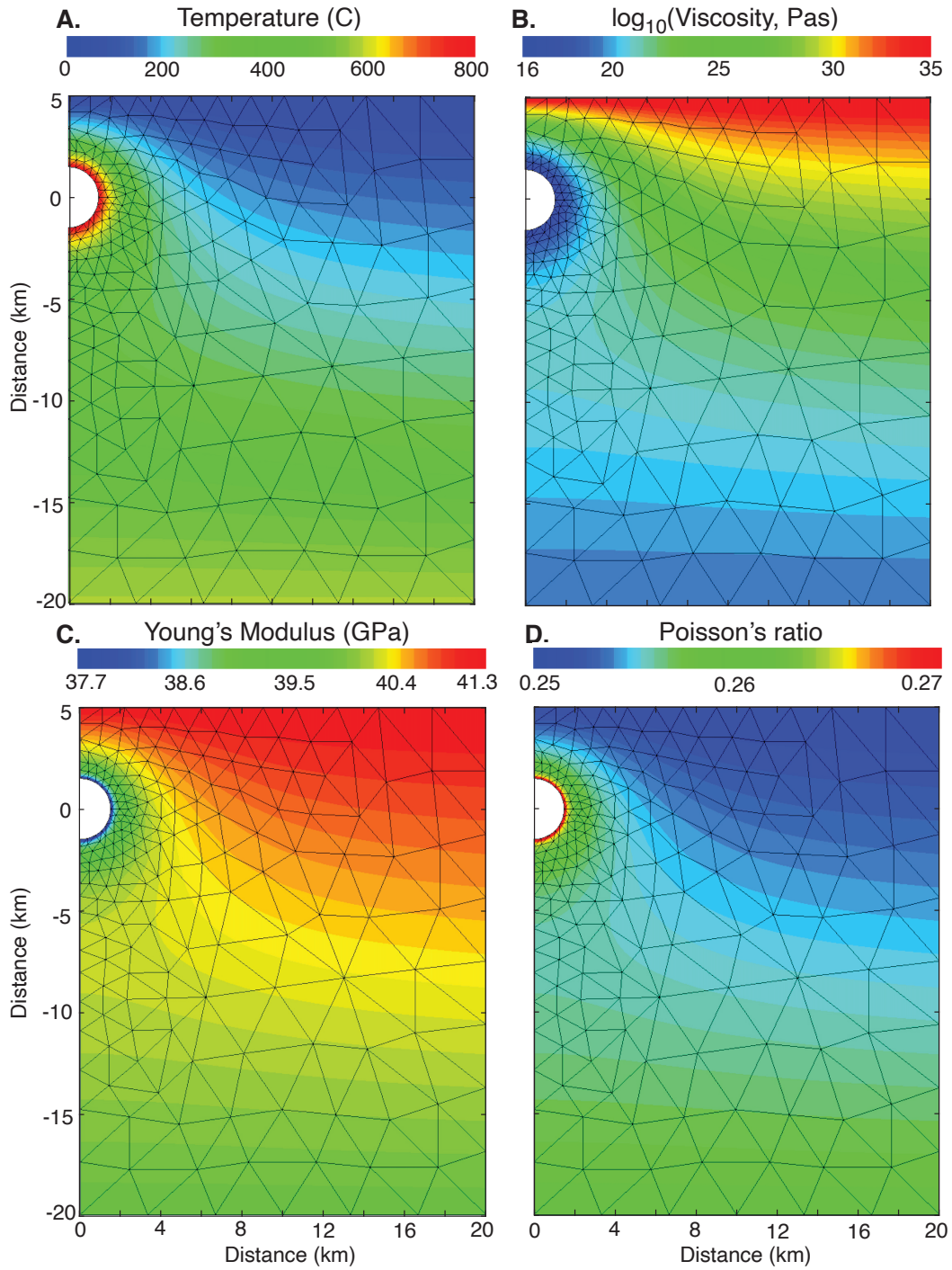


Figure 2. Material parameters used in our reference variable coefficients parameter study, with finite element mesh overlaid. **A.** Temperature, obtained by solving Equation 40 with $T_c = 800^\circ\text{C}$, surface temperature $T_s = 0^\circ\text{C}$, and geothermal gradient $\alpha = 20^\circ\text{C}/\text{km}$. **B.** Viscosity from Equation 43. **C.** Young's Modulus from Equation 44. **D.** Poisson's ratio from Equation 45.

443 displacements vanish at the far boundary, namely

$$444 \quad \sigma(x = 0, t) = \sin(\omega t), \quad (48a)$$

$$445 \quad u(x = L, t) = 0. \quad (48b)$$

446 We consider $t > 0$; the aging law Equation 47b thus requires an initial viscous strain
447 to be specified, which we express in general terms

$$448 \quad \gamma(x, t = 0) = \gamma_0(x), \quad (49)$$

449 where γ_0 as a given function. The Maxwell model thus gives rise to an initial-boundary
450 value problem defined by Equations 46-49.

451 We are interested in the response between stress and strain at the reservoir bound-
452 ary, with the expectation that viscous relaxation will lead to a phase difference. To do
453 this analysis it is useful to work with Hooke's law in rate form, namely,

$$454 \quad \dot{\epsilon} = \frac{1}{\mu} \dot{\sigma} + \frac{1}{\eta} \sigma. \quad (50)$$

455 Following Golden and Graham (1988), application of the Fourier transform to Equation
456 50 yields the constitutive law in frequency space

$$457 \quad \hat{\sigma}(\omega) = \hat{\mu}(\omega) \hat{\epsilon}(\omega), \quad (51)$$

458 which gives the usual relationship where stress is expressed as a function of strain through
459 a complex shear modulus $\hat{\mu}$ defined by

$$460 \quad \hat{\mu}(\omega) = \left(\frac{1}{\mu} - i \frac{1}{\eta\omega} \right)^{-1}. \quad (52)$$

461 The decomposition $\hat{\mu}(\omega) = \hat{\mu}_1(\omega) + i\hat{\mu}_2(\omega)$ into storage and loss moduli allows us to
462 express $\hat{\mu}$ as

$$463 \quad \hat{\mu}(\omega) = |\hat{\mu}(\omega)| e^{-i\delta} \quad (53)$$

464 where $\delta = -\tan^{-1}\left(\frac{\hat{\mu}_2}{\hat{\mu}_1}\right)$.

465 In our applications, however, we are interested in the strain response to an applied
466 (sinusoidal) stress, thus we must consider the constitutive relation Equation 51 in the
467 form

$$468 \quad \hat{\epsilon}(\omega) = \hat{d}(\omega) \hat{\sigma}(\omega), \quad (54)$$

469 where $\hat{d}(\omega) = 1/\hat{\mu}(\omega)$ is the complex creep modulus given by

$$470 \quad \hat{d}(\omega) = \frac{1}{\mu} - i \frac{1}{\eta\omega}, \quad (55)$$

471 which can be decomposed into $\hat{d}(\omega) = \hat{d}_1(\omega) + i\hat{d}_2(\omega)$ as before, and gives rise to the
472 similar form

$$473 \quad \hat{d}(\omega) = |\hat{d}(\omega)| e^{-i\beta}, \quad (56)$$

474 for $\beta = -\tan^{-1}\left(\frac{\hat{d}_2(\omega)}{\hat{d}_1(\omega)}\right)$. Applying the inverse Fourier transform to Equation 54 and
 475 using 48a yields

$$\begin{aligned}
 476 \quad \varepsilon(t) &= [d * \sigma](t), \\
 477 &= \hat{d}_1(\omega) \sin \omega t + \hat{d}_2(\omega) \cos \omega t, \\
 478 &= \sin(\omega t - \beta), \tag{57}
 \end{aligned}$$

479 which gives strain as an explicit function of stress, delayed by phase lag β . Since \hat{d} is chosen
 480 as the multiplicative inverse of $\hat{\mu}$ note that

$$481 \quad |\hat{d}(\omega)| = \frac{1}{|\hat{\mu}(\omega)|}, \tag{58a}$$

$$482 \quad \beta = -\delta, \tag{58b}$$

483 therefore the phase lag that strain experiences in response to an applied stress will be
 484 equal and opposite when reversing roles and considering stress in response to an applied
 485 strain. Note that we have used the sign convention for the phase lag such that positive
 486 values of β correspond to strain lagging behind stress.

487 To summarize, the strain response to a sinusoidal stress is also sinusoidal with a
 488 phase lag β , which can be simplified in terms of the Deborah number De by substituting
 489 in the real and imaginary parts of $\hat{d}(\omega)$, resulting in

$$490 \quad \beta = \tan^{-1}\left(\frac{1}{De}\right). \tag{59}$$

491 This analytic result provides insight into the physics of the viscoelastic model, as two
 492 limiting cases of the Deborah number (namely $De \rightarrow 0$ and $De \rightarrow \infty$) yield phase lags
 493 of 0 and $\pi/2$ (respectively) corresponding to the elastic and viscous limits (respectively).
 494 In addition, these analytic results can be generalized to higher dimensions which we do
 495 in the next section, providing useful code verification metrics as well as providing insight
 496 into the frequency response of more physically realistic modeling scenarios.

497 **4.2 Transfer Function and Analytic Signals**

498 The phase lag analysis for the 1D problem of the previous section can be gener-
 499 alized using the theory of Linear Time-Invariant (LTI) systems such as the viscoelastic
 500 problem we consider here. For general LTI systems, one can characterize some output
 501 signal $y(t)$ as the linear transformation of a system input $x(t)$, where we consider one-
 502 sided signals (i.e. they are 0 for $t < 0$) (Schetzen, 2003). The response y can be deter-
 503 mined as a convolution of the input x with the system impulse response h , namely

$$\begin{aligned}
 504 \quad y(t) &= (x * h)(t) \\
 505 &= \int_0^t x(t')h(t-t') dt'. \tag{60}
 \end{aligned}$$

506 The transfer function connecting the output signal $y(t)$ given the input signal $x(t)$ we
 507 denote $H\{y(t)|x(t)\}(i\omega)$, however we drop the argument within curly braces or func-
 508 tional dependence within parenthesis when these is implied via context. The transfer func-
 509 tion is defined as

$$\begin{aligned}
 510 \quad H(i\omega) &= \mathcal{L}\{h\}(i\omega) \\
 511 &= \frac{\mathcal{L}\{y\}}{\mathcal{L}\{x\}}(i\omega), \tag{61}
 \end{aligned}$$

512 where \mathcal{L} denotes the Laplace transform (a function of the complex variable s) and we
 513 have evaluated at $s = i\omega$. The transfer function thus provides the amplitude of the sys-
 514 tem output as a function of frequency of the input signal. As an example, Equation 54
 515 illustrates how $\hat{d} = H\{\varepsilon(t)|\sigma(t)\}$, i.e the transfer function when stress is the input sig-
 516 nal and strain is the output.

517 The specific input signal $x(t) = e^{i\omega t}$, for example, is called a characteristic func-
 518 tion as the response signal is given by

$$519 \quad y(t) = e^{i\omega t}H(i\omega), \tag{62}$$

520 indicating that the output signal is simply a scaling of $x(t)$ by $H(i\omega)$. If we consider spe-
 521 cific input and output signals $x(t) = A_{in} \sin(\omega t)$ and $y(t) = A_{out} \sin(\omega t - \phi)$, then we
 522 can use the Laplace transform to calculate the transfer function, namely,

$$\begin{aligned}
 523 \quad H(i\omega) &= \frac{A_{out}}{A_{in}} \frac{(-s \sin(\phi) + \omega \cos(\phi))/(s^2 + \omega^2)}{\omega/(s^2 + \omega^2)} \Bigg|_{s=i\omega} \\
 524 &= \frac{A_{out}}{A_{in}} e^{-i\phi}, \tag{63}
 \end{aligned}$$

525 i.e. a constant, independent of ω . Performing an inverse Laplace transform indicates that
 526 the corresponding system impulse response is a delta function, namely, $h(t) = (A_{out}/A_{in})\delta(t -$
 527 $\phi/\omega)$.

528 Equations 63-63 illustrate the important point that evaluation at $s = i\omega$ must take
 529 place after the ratio is computed, so that the poles in the Laplace transforms of the si-
 530 nusoids x and y are removed. In numerical studies making use of the discrete Fourier
 531 transform, this evaluation cannot be done after the ratio is computed, which can lead
 532 to division by zero. An alternative means for defining the transfer function therefore is
 533 via the concept of analytic signals, which have straight-forward numerical approxima-
 534 tions and avoid potential division by zero.

535 Analytic signals are defined in the following manner. Consider the real valued sig-
 536 nal $z(t)$ and denote its Fourier transform by $\hat{z}(\xi)$. Define the function

$$537 \quad \hat{z}_a(\xi) = 2\mathcal{H}(\xi) \hat{z}(\xi) \tag{64}$$

(where \mathcal{H} is the Heaviside step function), which contains only the non-negative frequency components of $\hat{z}(\xi)$. The analytic signal corresponding to z , denoted $z_a(t)$, is a complex-valued function obtained by transforming \hat{z}_a back to the time domain using the inverse Fourier transform, yielding

$$z_a(t) = z(t) + i\mathbb{H}\{z\}(t), \quad (65)$$

where \mathbb{H} is the Hilbert transform. Properties of Hilbert transforms mean that for input signal $x(t)$ and response signal $y(t)$ of an LTI system, we have that

$$y_a(t) = (h * x_a)(t). \quad (66)$$

Considering the analytic signals $x_a(t) = A_{\text{in}}e^{i\omega t}$ and $y_a(t) = A_{\text{out}}e^{i(\omega t - \phi)}$ associated with the input and output signals under consideration, we have that

$$A_{\text{out}}e^{i(\omega t - \phi)} = A_{\text{in}}e^{i\omega t}H(i\omega). \quad (67)$$

This results in the transfer function

$$H(i\omega) = \frac{A_{\text{out}}}{A_{\text{in}}}e^{-i\phi}, \quad (68)$$

previously obtained using Laplace transforms. The amplitude $|H| = \left|\frac{A_{\text{out}}}{A_{\text{in}}}\right|$ is often referred to as the gain because it describes how the frequency content in the output signal is amplified in response to the input. And finally, $\phi = -\arg(H)$ is the phase lag, which agrees with that of the 1D Maxwell model considered in the previous section. Following the notation for the transfer function, we let $\phi\{y(t) | x(t)\}$ denote the phase lag between the output signal $y(t)$ given the input signal $x(t)$, but drop the argument in curly braces when it is implied via context.

4.3 Numerical Calculations of the Transfer Function

The analytic signal corresponding to a real, discrete time-series is implemented in the Python SciPy library via the `scipy.signal.hilbert()` function. The transfer function connecting an input signal $x(t)$ to output signal $y(t)$ is computed via the ratio of corresponding analytic signals, from which we can compute phase and amplitude. All scripts are available in the code repository. In practice, there exists an initial spin-up period (~ 4 cycles) before solutions settle into a sinusoidal response and it is necessary to compute the transfer function once out of this phase.

In addition to the spin-up phase, the output signal can be shifted to oscillate around a non-zero value, which can complicate the calculation of the phase lag using our numerical techniques. The 1D analysis of the previous section illustrates why this occurs. Specifying the initial condition Equation 49 impacts the evolution of the displacement and

570 stress fields in the following way: suppose $\gamma_0(x) = 0$ for each $x \in [0, L]$. We can sim-
 571 plify the boundary condition Equation 48 by taking $P_0 = \omega = 1$. The sinusoidal pres-
 572 sure imposed at the left boundary along with Equation 47a imply a uniform stress field

$$573 \quad \sigma(t, x) = \sin t. \quad (69)$$

574 Integrating Equation 47b yields the viscous strain

$$575 \quad \gamma(t) = -\frac{1}{\eta} \cos t + \frac{1}{\eta}, \quad (70)$$

576 and solving Equation 47c for total strain gives the solution

$$577 \quad \varepsilon(t) = \frac{1}{\mu} \sin t - \frac{1}{\eta} \cos t + \frac{1}{\eta}, \quad (71)$$

578 which illustrates how the strain response is sinusoidal with a shift of $1/\eta$. Although strain
 579 starts initially at 0, it fluctuates around the non-zero value $1/\eta$, corresponding to a vol-
 580 ume change (length change in 1D). To avoid this situation, one could specify a differ-
 581 ent initial viscous strain, i.e. $\gamma_0(x) = -1/\eta$ which would yield the a strain response fluc-
 582 tuating around zero. In the 2D problems considered in this work, it is difficult to know
 583 a priori the initial viscous strain that would preclude a volume change. Thus to com-
 584 pare the phase-lag response, fields that do not fluctuate around zero must first be shifted
 585 to do so. The spin-up phase contributes an exponentially decaying component in the out-
 586 put signal, therefore we calculate approximate phase and amplitude after 4 pressuriza-
 587 tion cycles.

588 The sinusoidal pressure forcing we impose at the reservoir wall given by Equation
 589 17a is considered the input signal $P(t)$ for all of our studies. To verify correctness of our
 590 numerical methods, we first consider as the output signal the normal component of strain
 591 at a single spatial point on the wall, namely $\varepsilon_{rr}(r = a, z = 0, t)$. Because at the reser-
 592 voir wall the stress-strain relation effectively reduces to a 1D problem at a point, our nu-
 593 meric calculations are verified by comparing our numerical calculations of transfer func-
 594 tion amplitude and phase lag against the theoretical stress-strain relationship for a Maxwell
 595 material for different forcing periods τ (see Equation 19), as evidenced in Figure 3. In
 596 addition we compute the phase lag observed in the vertical component of displacement
 597 at Earth's surface $u_z(r = 0, z = D + b, t)$ as well as the transfer function amplitude
 598 (gain).

599 **5 Computational Results**

600 Viscoelastic behavior of magma reservoirs is often characterized in terms of defor-
 601 mation of a flat free surface induced by pressurization of a spheroidal reservoir (e.g., Segall,

Table 1. Parameters used in Applications (unless otherwise noted).

Symbol	Explanation	Value
a	Ellipse semi-major axis	1500 m
b	Ellipse semi-minor axis	1500 m
D	Reservoir depth beneath Earth's surface	3500 m
L_r	Domain length	20000 m
L_z	Domain length	20000 m
P_0	Pressure amplitude	10 MPa
A_D	Dorn parameter	10^9 Pa s
A	Material-dependent constant for viscosity	4.25×10^7 Pa s
E_a	Activation energy	141 kJ/(mol)
R	Boltzmann's molar gas constant	8.314 J/(mol K)
T_c	Reservoir Temperature	800°C
T_s	Surface temperature	0°C
α	Geothermal gradient	20°C/km
ν_{\min}	Min Poisson's ratio	0.25
ν_{\max}	Max Poisson's ratio	0.49
E_{\max}	Max Young's modulus	4.0×10^{10} Pa
c_1	parameter in model for E	1.8×10^{10} Pa
c_2	parameter in model for E	-3.5×10^6 Pa/°C
c_3	parameter in model for E	4.3×10^9 Pa
s	parameter in model for E	120 °C
\bar{T}	Temperature threshold	924°C

2016; Head et al., 2019; Townsend, 2022). Even in this relatively simple case, the problem is complex because a large number of control parameters matter and trade off in non-unique ways to generate surface deformation patterns. An additional challenge is that the problem is generally not amenable to analytic analysis such as has been conducted in simplified limits (Dragoni & Magnanensi, 1989; Karlstrom et al., 2010; Bonafede et al., 1986).

Our computational framework is fairly general, but we will focus on a specific and relatively unexplored part of this problem here, the frequency dependence of surface de-

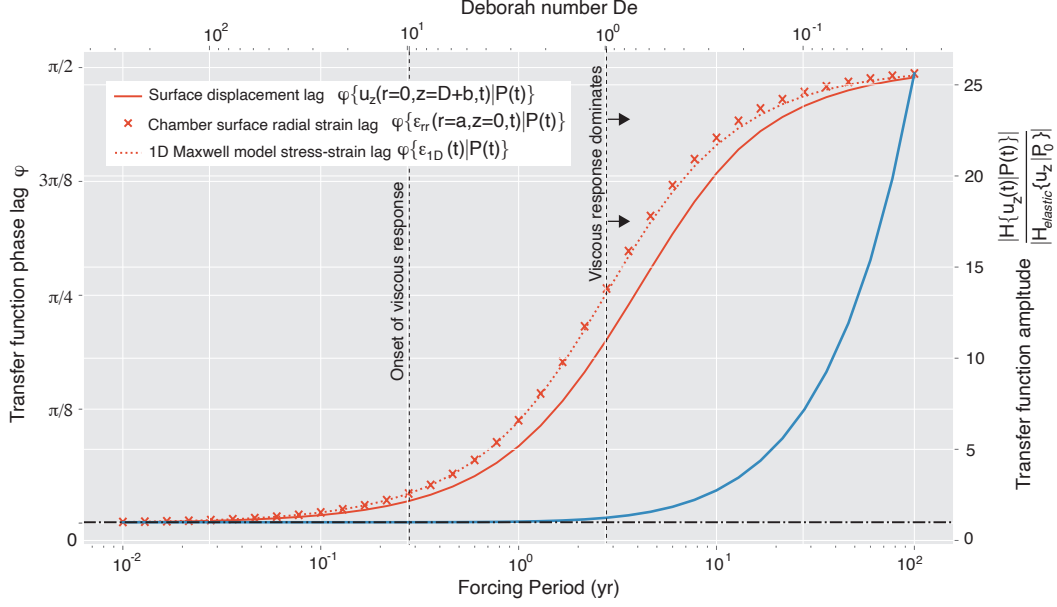


Figure 3. Phase lag ϕ of the transfer function between reservoir pressure and radial strain at the reservoir wall ($\phi\{\epsilon_{rr}(r = a, z = 0, t|P(t))\}$, red dashed curve) and vertical displacement at the surface overlying the reservoir ($\phi\{u_z(r = 0, z = D + b, t|P(t))\}$, solid red curve). Crosses come from the 1D analytic prediction (Equation 59). Right axis and blue curve plot the amplitude of the transfer function $|H\{u_z(r = 0, z = D + b, t|P(t))\}|$ normalized by the transfer function amplitude in a purely elastic limit (which uses the same averaged elastic coefficients but with $\eta = 1 \times 10^{34}$ making viscous effects negligible). Upper x axis is the Deborah number, lower x-axis dimensionalizes into period of sinusoidal pressure forcing using $\eta = 2.20 \times 10^{17}$ Pas, $\lambda = 16.7$ GPa and $\mu = 16.0$ GPa. Vertical dashed lines correspond to threshold Deborah numbers associated with onset of viscous response in host rocks.

610 formation. All fixed parameters used in this study are listed in Table 1, unless otherwise
 611 noted. In the constant coefficient case studied in Figure 3 (a spheroidal reservoir in a
 612 uniform viscoelastic halfspace), sinusoidal forcing at the reservoir wall results in surface
 613 deformation patterns that are simply parameterized in terms of the Deborah number (Equa-
 614 tion 59). $De = 10$ signifies the onset of viscous response in host rocks, while for $De <$
 615 1 the host rock response is dominantly viscous in the sense that phase lag ϕ between sur-
 616 face deformation is more than halfway to the viscous limit.

617 The constant coefficient case we extract from the general (variable coefficient) case
 618 by choosing constant values of elastic parameters μ and λ by spatially averaging the sub-
 619 sequent non-constant coefficient calculations (Figure 3, bottom axis). For viscosity we
 620 suppose that a forcing period of 1 year yields a surface phase lag of 0.3 rad. From this
 621 phase lag we compute the associated Deborah number and solve Equation 28 for viscos-
 622 ity. The resulting constant material parameters are: $\mu = 16.0\text{GPa}$, $\lambda = 16.7\text{GPa}$, $\eta =$
 623 $2.20 \times 10^{17}\text{Pas}$. We can then associate a Deborah number De with a forcing period τ
 624 via Equation 28 and examine the transition to a viscous response as a function of forc-
 625 ing period. In this example $\tau = 1$ yr corresponds to maximum surface displacement that
 626 lags behind maximum chamber pressure by ~ 16 days at similar amplitude to the elas-
 627 tic limit, while $\tau = 10$ yr corresponds to a phase lag of ~ 1.9 years with $\sim 3\times$ ampli-
 628 tude to the elastic limit.

629 However, uniform viscosity is a poor approximation to crustal rheology in magmatic
 630 regions. To understand what changes with more realistic temperature-dependent viscos-
 631 ity and elastic constants, we now study how pressure forcing period affects ground de-
 632 formation in the variable coefficient problem outlined in Section 3.3.

633 Figure 4 shows the time series of maximum vertical surface displacement and ra-
 634 dial strain at the reservoir wall (plotted versus angular frequency ω) for several repre-
 635 sentative forcing periods. Figure 5 plots the spatial variation in vertical and horizontal
 636 components of surface displacements u_z, u_r as well as the scalar von Mises stress $\sigma_v =$
 637 $\sqrt{3J_2}$ with J_2 the second deviatoric stress invariant for four positions in the pressure cy-
 638 cle ($\omega = 0, \pi/2, \pi, 3\pi/2$ radians) and three forcing periods. Finally, Figure 6 shows the
 639 transfer function phase $\phi\{u_z(r = 0, z = D + b, t) | P(t)\}$ and normalized amplitude
 640 $|H\{u_z(r = 0, z = D + b, t) | P(t)\}|/H_{elastic}\{u_z(r = 0, z = D + b) | P_0\}$ for a sweep
 641 through pressure forcing period τ . Transfer function results are computed for two choices
 642 of reservoir temperature $T_c = 800, 900^\circ\text{C}$ in Figure 6.

643 In contrast to the constant coefficient case, Figures 4-6 demonstrate that temper-
 644 ature dependent material parameters strongly impact the viscoelastic response of the sys-

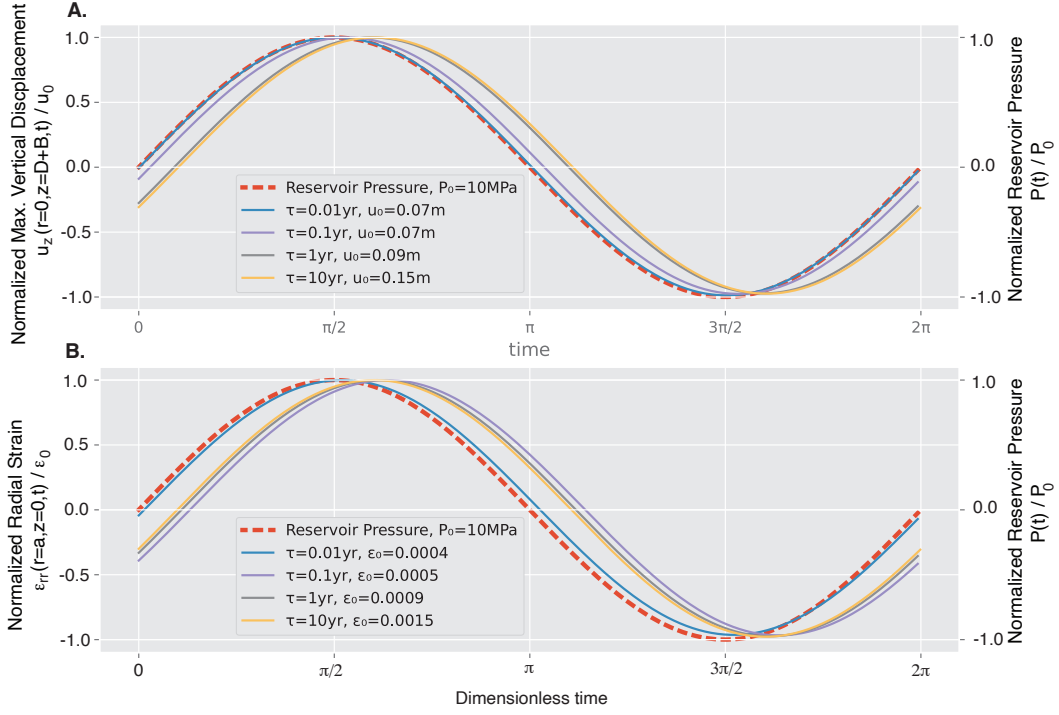


Figure 4. Temporal evolution (time non-dimensionalized by τ) associated with non-constant coefficient simulations at select forcing periods. Colored curves correspond to different forcing periods and normalization amplitudes u_0, ϵ_0 . **A.** Normalized maximum vertical surface displacement. In dimensional time, peak vertical surface displacement for $\tau = 0.01, 0.1, 1, 10$ years occurs 10.0 min, 12.7 hr, 17.6 days, and 6.3 months after peak reservoir pressure, respectively, associated with phase lags $\phi\{u_z(r = 0, z = D + b, t|P(t))\} = 0.012, 0.091, 0.303$ and 0.331 radians. **B.** Normalized radial strain at the cavity wall. We see that phase offset at the chamber wall differs from that seen at the surface.

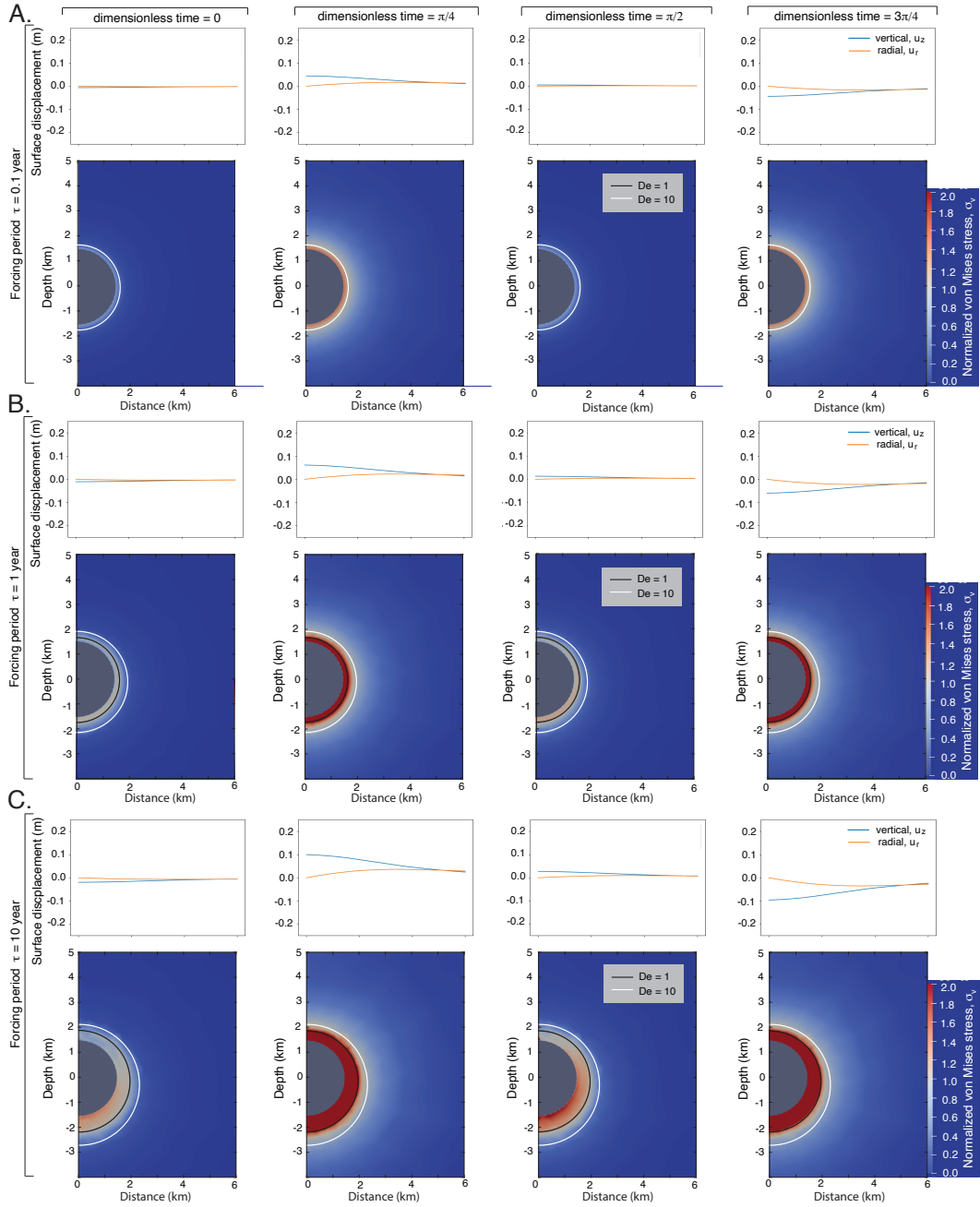


Figure 5. Spatial pattern of surface displacements u_z, u_r (top lines) and subsurface distribution of von Mises stress σ_v (bottom colors, normalized by $P_0 = 10$ MPa) for dimensionless times $0, \pi/4, \pi/2, 3\pi/4$ during a pressure cycle. Black contour is $De = 1$, white contour is $De = 10$. **A.** Forcing period $\tau = 0.1$ yr, max $\sigma_v = 20.9$ MPa. **B.** Forcing period $\tau = 1$ yr, max $\sigma_v = 42.2$ MPa. **C.** Forcing period $\tau = 10$ yr, max $\sigma_v = 100.7$ MPa. Supplemental movies S1-S3 show time evolution of these simulations in more detail.

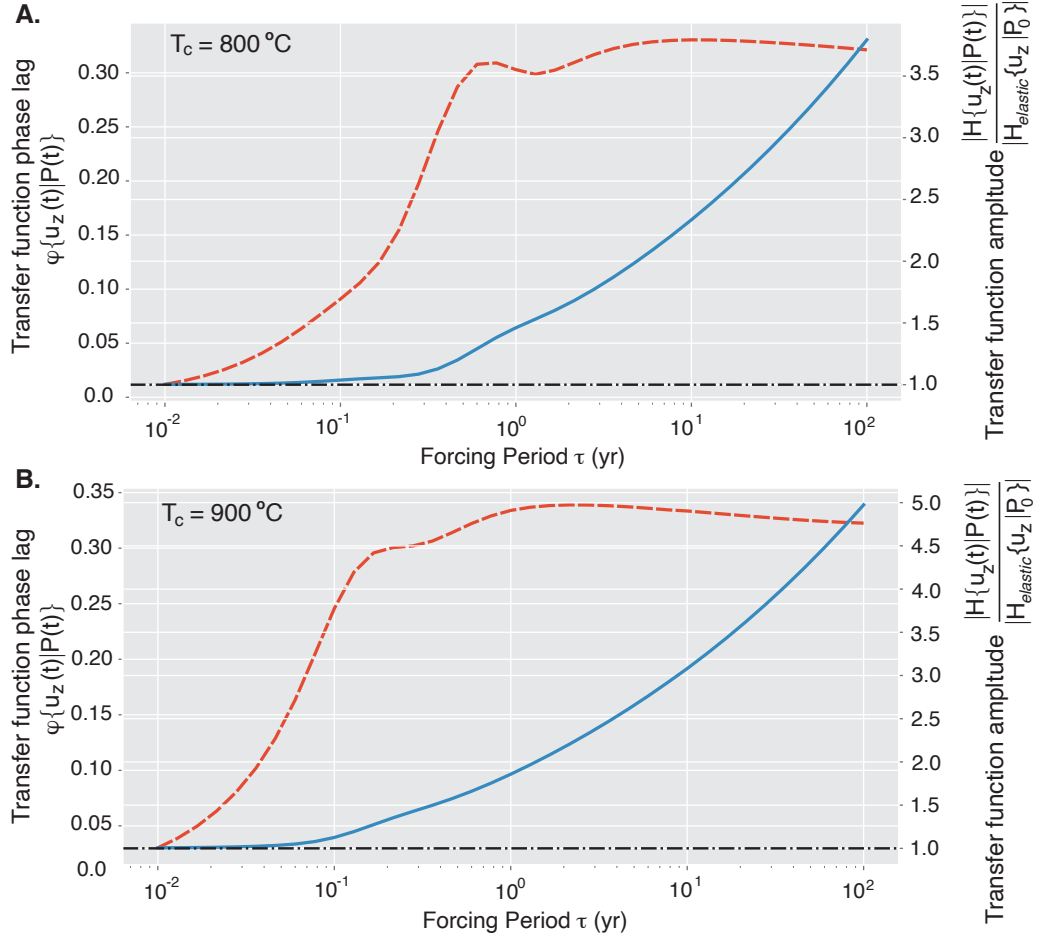


Figure 6. Transfer function phase lag $\phi\{u_z(r = 0, z = D + b, t)|P(t)\}$ (in radians, left axes) and amplitude $|H\{u_z(r = 0, z = D + b, t)|P(t)\}|$ (right axes, normalized by the variable coefficient elastic case $|H_{elastic}\{u_z(r = 0, z = D + b)|P_0\}|$ extracted from the variable coefficient viscoelastic case with $\eta = 1 \times 10^{34}\text{Pas}$), as a function of pressure forcing period. **A.** Reservoir temperature of $T_c = 800^\circ\text{C}$. **B.** Reservoir temperature of $T_c = 900^\circ\text{C}$.

645 tem. Most pronounced is a saturation of phase lag at ~ 0.3 radians and muted ampli-
 646 fication of displacements relative to the constant coefficient case. As evidenced by the
 647 large σ_v (which measures deviatoric shear stress magnitude), viscous effects are confined
 648 near the reservoir wall. This results in more pronounced mechanical lag at the reservoir
 649 wall than at the surface (Figure 4) and concentration of shear stress σ_v through the cy-
 650 cle in a narrow aureole around the chamber (Figure 5).

651 The strong spatial variability in material parameters now implies a spectrum of Maxwell
 652 relaxation times and hence spatially variable Deborah number. We see that a local value
 653 of De still characterizes the region experiencing significant viscous strain. Figure 5 shows
 654 that $De = 10$ effectively bounds the region experiencing significant von Mises stress in
 655 excess of chamber overpressure P_0 , with $De = 1$ once again a measure of the shell cen-
 656 troid. For small forcing periods the shell is significantly reduced ($De = 1$ does not ap-
 657 pear for $\tau = 0.1$ year forcing period). Both contours are asymmetric with depth due
 658 to the geothermal gradient.

659 To isolate viscous effects, the transfer amplitudes for Figure 6 are normalized us-
 660 ing the variable coefficient elastic limit. That is, elastic parameters are computed using
 661 a thermal profile but viscosity $\eta = 1 \times 10^{34} \text{Pa} \cdot \text{s}$. Then this variable coefficient elastic
 662 problem is simulated for 10 cycles and a transfer function $H_{elastic}$ is computed from the
 663 output.

664 The transfer function curves in Figure 6 also have more complex structure than their
 665 constant coefficient counterpart in Figure 3. The phase lag $\phi\{u_z(r = 0, z = D+b, t) | P(t)\}$
 666 is non-monotonic, with two local maxima superimposed on a sigmoidal increase from 0
 667 to ~ 0.3 radians over three orders of magnitude in forcing period. Increasing the reser-
 668 voir temperature from 800°C to 900°C shifts this phase lag curve to shorter periods and
 669 increases the maximum phase lag, which suggests that the local maxima are due in part
 670 to an expanded viscous shell around the reservoir (i.e., larger region where $De < 10$).
 671 As will be discussed in the next section, we speculate that non-monotonic phase lag at
 672 longer period occurs because larger regions of the domain begin to contribute to the sur-
 673 face displacements.

674 The plateau seen in the phase lag in Figure 6 is not mirrored by the amplitude of
 675 displacements. Relative to the elastic limit, the blue curves show a continuous increase
 676 in maximum displacements at increasing τ , mirrored by the spatial pattern of u_z and
 677 u_r in Figure 5. There is an inflection point that corresponds to the first local minimum
 678 in ϕ , but viscous amplification is otherwise a monotonically increasing function of τ , with
 679 amplification factors at 100 yr forcing period $\sim 3.7\times$ and $\sim 5\times$ for 800°C and 900°C cham-

680 ber temperatures. At small τ the amplification factor is asymptotic to the variable co-
 681 efficient elastic limit.

682 **6 Discussion**

683 This work makes two primary contributions. First, we develop a rigorous numer-
 684 ical framework based on a high-order finite element method for the computation of de-
 685 formation and stress around axisymmetric magma reservoirs. Second, we study a par-
 686 ticular problem relevant to volcanism - sinusoidal pressurization/depressurization of a
 687 spherical reservoir in a half-space - and demonstrate how surface deformation patterns
 688 are frequency dependent. This section is organized into a discussion associated with each
 689 contribution.

690 **6.1 Computational Considerations for Time-evolving Magmatic Systems**

691 Although numerous authors have studied viscoelastic behavior in magmatic sys-
 692 tems numerically, we are unaware of a systematic analysis of the numerical and compu-
 693 tational issues associated with this problem. As volcanic deformation datasets become
 694 better resolved in space and time, and as magma reservoir models are generalized to in-
 695 clude more physical processes, neglecting these numerical and computational consider-
 696 ations is likely to be a major factor limiting scientific progress.

697 We derived conditions on the time step, which guarantees stability of the aging law,
 698 and showed that the numerical solution converges to the exact solution at the theoret-
 699 ical rates of convergence in both space and time. However, in practice, even these 2D
 700 simulations are computationally expensive because a system of equations (the discretized
 701 equilibrium equation) must be solved at each time step, and this constitutes the bulk
 702 of the computational load. We perform a direct solve of the system while it's still pos-
 703 sible to hold the matrix factorization in system memory. For larger problems (e.g. in 3D
 704 or with larger domains sizes or if a finer spatial resolution is required), matrix-free it-
 705 erative methods on parallel machines would be necessary (Chen et al., 2022). Further-
 706 more, if the relevant time scale of interest is the forcing period τ , which can be much longer
 707 than the minimum viscous relaxation time η/μ (so that $De \ll 1$), the problem can be-
 708 come arbitrarily numerically stiff: very small time steps are required for numerical sta-
 709 bility, much smaller than that required to accurately resolve the sinusoidal pressure forc-
 710 ing.

711 To address this corresponding computational burden, an implicit time stepping scheme
 712 (such as backward Euler) would need to be applied, or alternative schemes such as split-

713 ting algorithms (Carcione & Quiroga-Goode, 1995). For problems in which total strains
 714 are large (e.g., dominated by viscous flow) it may also be advantageous to reformulate
 715 the governing equations in terms of split viscous and elastic strain rates (rather than strains),
 716 as is commonly done in mantle dynamics models (e.g., Moresi et al., 2002). A disadvan-
 717 tage of this approach is that elastic stresses are less explicitly resolved, which is not ac-
 718 ceptable for the present application.

719 One drawback of our method is that it is not robust in the incompressible limit ($\nu =$
 720 0.5). More sophisticated locking-free techniques—see e.g., Gopalakrishnan and Guzmán
 721 (2012)—could be employed to solve the equilibrium equations stably in the incompress-
 722 ible limit, as could be needed for fully coupled fluid-solid magmatic models. To apply
 723 our computational framework to the study of more physically realistic problems might
 724 require further numerical developments. The inclusion of boundary tractions (to repre-
 725 sent topography for example, or background tectonic stress) can be explored here directly
 726 by setting specific values of the boundary data. But more realistic time-evolving quan-
 727 tities, for example a sawtooth pressure at the reservoir wall such as would be expected
 728 for eruption cycles (Cianetti et al., 2012), may require adaptive time-stepping techniques
 729 to integrate efficiently through regions of both slow and fast evolution, similar to meth-
 730 ods used in models for long-term earthquake activities (e.g., Erickson & Dunham, 2014).

731 **6.2 Frequency Dependent Magmatic Deformation**

732 We have studied here a magma chamber problem that, while simple in some re-
 733 spects, has a strong basis in past observations and represents a template for future ad-
 734 vances. In the elastic limit, corrections for less idealized geometry and material hetero-
 735 geneity are fairly well known (Segall, 2010), and elastic parameter trade-offs have been
 736 explored to some extent (e.g., Currenti & Williams, 2014). But viscoelastic behavior is
 737 far less well understood. Case studies have demonstrated important trade-offs in geom-
 738 etry, constitutive law, and thermal state (Segall, 2019; Head et al., 2019, 2021), but gen-
 739 eral time-dependence introduces significant complexities.

740 The cyclic forcing studied here represents a powerful framework to explore phenomenol-
 741 ogy of transient magma chamber deformation. While magma pressure histories are not
 742 generally sinusoidal, linear viscoelasticity (in any form, not just the Maxwell model) im-
 743 plies that arbitrary forcing histories may be constructed through appropriate superpo-
 744 sition.

745 As a specific example, consider a reservoir pressure history (the input signal) given
 746 by the 2τ -periodic rectangular pulse of unit width

$$747 \quad P(t) = P_0 (\mathcal{H}(t) - \mathcal{H}(t - 1)). \quad (72)$$

748 with $\tau > 1$. The complex Fourier series representation for $P(t)$ can be expressed as

$$749 \quad P(t) = \sum_{n=-\infty}^{\infty} c_n e^{i\omega_n t}, \quad (73)$$

750 where $\omega_n = n\pi/\tau$ and the complex Fourier coefficients are given by

$$751 \quad c_n = P_0 \frac{1}{\tau\omega_n} e^{-i\omega_n/2} \sin(\omega_n/2). \quad (74)$$

752 Then the output signal $y(t)$ can be expressed in terms of its Fourier series

$$753 \quad y(t) = \sum_{n=-\infty}^{\infty} d_n e^{i\omega_n t} \quad (75)$$

754 with coefficients

$$755 \quad d_n = H(i\omega_n) c_n, \quad (76)$$

756 i.e. the coefficients of the input signal, scaled by the transfer function H . This exam-
 757 ple demonstrates that sequences of impulsive pressure changes (such as eruptions) that
 758 are non-harmonic in time can still be characterized with the framework developed here.

759 As a second example, if the pressure history is given by a unit impulse at $t = t_0$,
 760 namely

$$761 \quad P(t) = P_0 \delta(t - t_0), \quad (77)$$

762 then Equation 60 implies that the output signal is simply

$$763 \quad y(t) = h(t - t_0), \quad (78)$$

764 i.e. the system impulse response. This pressure history represents a simple model for sud-
 765 den pressure perturbation (e.g., Segall, 2016). The implied ground deformation in this
 766 case is the impulse response function of the magmatic system.

767 Both examples imply that frequency-domain inversion for magmatic pressure his-
 768 tories from ground motions reduces to seeking weights for the forcing periods represented
 769 in Figure 6 to match general time-dependent deformation data. Further studies will be
 770 needed to see what degeneracies exist in the transfer function itself as control param-
 771 eters are varied.

772 An interesting challenge implied by our analysis is how to find initial conditions.
 773 Our time-dependent steady-state (purely oscillatory) implicitly starts from a unstressed
 774 state, but as illustrated through 1D analysis (Section 4) the initial strain determines the

775 equilibrium position around which steady viscoelastic oscillations occur. In the 2D vari-
 776 able coefficients case the choice of initial strain that will result in a particular chamber
 777 size (or geometry) is less trivially found - equilibrium magma chamber volume is not an
 778 independent parameter but rather a model outcome. From a geophysical perspective,
 779 this implies that absolute stress histories are needed to interpret general surface displace-
 780 ment timeseries at volcanoes, and could play an important role in eruption cycles as it
 781 does for earthquake cycles (e.g., Erickson et al., 2017).

782 Another important implication of this model is that the volume of crustal rock around
 783 the chamber that experiences viscous strain over a chamber pressure cycle depends on
 784 the frequency of forcing. As demonstrated by Figure 3, $De = 10$ effectively marks the
 785 onset of viscous host response to cycling pressure forcing. Figure 5 extends this to vari-
 786 able coefficients, suggesting that $De = 10$ effectively bounds the region in which sig-
 787 nificant deviatoric shear stresses (as measured by σ_v in excess of P_0) occur.

788 We suggest that the frequency-dependent $De = 10$ contour represents an effec-
 789 tive outer edge to the viscoelastic “shell” considered fixed in size by previous models for
 790 viscoelastic magma chamber mechanics (Dragoni & Magnanensi, 1989; Jellinek & De-
 791 Paolo, 2003; Karlstrom et al., 2010; Degruyter & Huber, 2014; Segall, 2016; Head et al.,
 792 2021; Liao et al., 2021). Our model demonstrates that viscoelastic shell size even for a
 793 steady temperature distribution depends on the time history of reservoir stress - like
 794 equilibrium reservoir size, it is a transient model output.

795 **6.3 Implications for Transcrustal Magmatic Systems**

796 Magma reservoirs that feed volcanic eruptions likely sit near the top of transcrustal
 797 magma transport networks characterized by high temperatures and partial melt (Sparks
 798 et al., 2017). Some of this magma accumulates episodically into high melt fraction reser-
 799 vairs such as we model here. But it is to be expected that, as transcrustal magma trans-
 800 port networks mature, a significant fraction of the crust is heated and remains hot for
 801 extended periods of time. What are the implications of this rheological structure for ground
 802 deformation?

803 We can begin to answer this question by noting that the bulk rheology of magma
 804 storage zones is frequency dependent, as has been recognized for crustal rheology in other
 805 settings (Lau & Holtzman, 2019). Figure 7 plots the $De = 10$ contour representing on-
 806 set of viscous mechanical response for different pressurization periods, from 0.1 to 1000
 807 years. We then consider end member steady state thermal regimes: chamber boundary

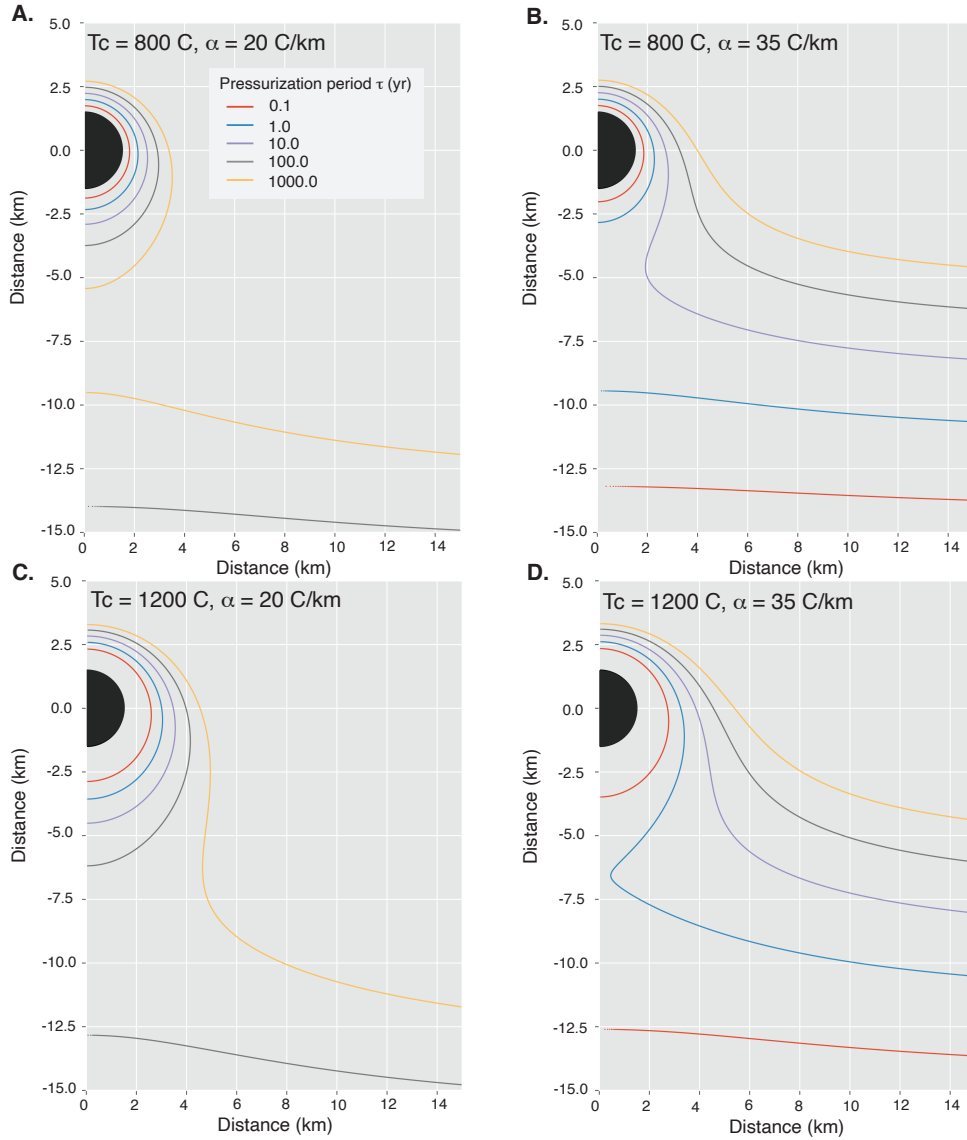


Figure 7. Spatial regions associated with a Deborah number $De = 10$ for varying periods τ of the forcing function (colored curves), illustrating end member thermal regimes. Magma reservoir is black semi-circle in all panels. **A.** Reservoir temperature $T_c = 800^\circ\text{C}$ with geothermal gradient $\alpha = 20^\circ\text{C}/\text{km}$. **B.** Reservoir temperature $T_c = 800^\circ\text{C}$ with geothermal gradient $\alpha = 35^\circ\text{C}/\text{km}$. **C.** Reservoir temperature $T_c = 1200^\circ\text{C}$ with geothermal gradient $\alpha = 20^\circ\text{C}/\text{km}$. **D.** Reservoir temperature $T_c = 1200^\circ\text{C}$ with geothermal gradient $\alpha = 35^\circ\text{C}/\text{km}$.

808 temperature of $T_c = 800^\circ\text{C}$ and 1200°C , and geothermal gradient of $\alpha = 20^\circ\text{C}/\text{km}$
 809 and $35^\circ\text{C}/\text{km}$.

810 In the cold extreme (Figure 7A), we see that viscoelastic behavior is confined to
 811 a shell around the chamber in all but 1000 year forcing. This is consistent with commonly
 812 used models of isolated magma chambers. At long periods however the mid/lower crust
 813 is activated and starts to creep, defining a mid-crustal brittle-ductile transition that de-
 814 pends on background geothermal gradient. In the hot extreme (Figure 7D), we see that
 815 viscoelastic response of the near-chamber region extends continuously into the mid-crust
 816 for forcing periods as low as 10 years. This defines a spatially coherent viscous domain
 817 induced by magmatic heating (Karlstrom et al., 2017), activated by long-period forcing.
 818 While we leave further exploration of this to future work, we note that some of the struc-
 819 ture seen in phase lag variations at periods of $\sim 10 - 100$ years in Figure 6 likely re-
 820 flect changes to the shape as well as radial extent of the viscous shell. Because magma
 821 transport is likely unsteady at many scales, ground deformation in volcanic regions will
 822 include contributions from viscoelastic deformation defining the crustal thermo-rheologic
 823 footprint of magmatism on a range of timescales.

824 Appendix A Verification via Convergence Tests

825 We verify the accuracy of our numerical method using the method of manufactured
 826 solutions (Roache, 1998) and explain this technique in the context of the dimensional
 827 problem (computationally we solve the non-dimensionalized problem). This verification
 828 technique lets us choose arbitrary solution fields $u^*(r, z, t), C^*(r, z, t)$ to act as exact so-
 829 lutions necessary for measuring convergence. u^* and C^* satisfy the governing equations
 830 and boundary conditions with particular choices of source terms and boundary data which
 831 we detail in this section.

832 We choose a manufactured solution to the initial-boundary-value problem Equa-
 833 tion (1a),(4)-(8) based on the well-known solution to the pressurized magma cavity prob-
 834 lem in an elastic half-space (Mogi, 1958; Segall, 2010) given by

$$835 \quad \mathbf{u}_e = \frac{P_0 a^3}{4\mu(r^2 + z^2)^{3/2}} \begin{bmatrix} r \\ z \end{bmatrix}. \quad (\text{A1})$$

836 which satisfies the reservoir pressure conditions Equations (17a)-(17b). Define the man-
 837 ufactured solutions u^*, C^* by

$$838 \quad u^*(r, z, t) = (2 - e^{-t})\mathbf{u}_e, \quad (\text{A2})$$

$$839 \quad C^*(r, z, t) = (1 - e^{-t})\mathbf{E}\underline{\underline{\epsilon}}(\mathbf{u}_e), \quad (\text{A3})$$

Table A1. Parameters used in Convergence Tests and their Symbols.

Symbol	Explanation	Value
a	Ellipse semi-major axis	4 km
b	Ellipse semi-minor axis	4 km
D	Reservoir depth beneath Earth's surface	4 km
L_r	Domain length	10 km
L_z	Domain depth	10 km
μ	shear modulus	0.5 GPa
λ	Lamé's first parameter	4 GPa
η	Viscosity	0.5 GPa-s
P_0	Chamber Pressure	10 GPa

Table A2. Spatial convergence data, measured with respect to the discrete L^2 -norm, for a single time step of $\Delta t = 10^{-7}$ using polynomials of degree 3.

h	$\ \underline{\mathbf{C}} - \underline{\mathbf{C}}_h\ $	$\underline{\mathbf{C}}$ -rate	$\ \mathbf{u} - \mathbf{u}_h\ $	\mathbf{u} -rate
$h/2$	5.25×10^{-9}		1.84×10^{-8}	
$h/4$	7.17×10^{-10}	2.87	1.31×10^{-9}	3.81
$h/8$	9.13×10^{-11}	2.97	8.41×10^{-11}	3.96
$h/16$	1.14×10^{-11}	3.00	5.24×10^{-12}	4.00

840 which satisfies equilibrium and specifies all boundary data. It does not however satisfy
 841 the aging law, and to correct for this discrepancy a source term is added, namely

$$842 \quad \underline{\dot{\mathbf{C}}} = \mathbf{E} \mathbf{A} \underline{\dot{\boldsymbol{\sigma}}} + \mathbf{G}. \quad (\text{A4})$$

843 Here, the source term \mathbf{G} is determined from the manufactured solutions to be

$$844 \quad \mathbf{G} = e^{-t} \boldsymbol{\sigma}^* - \frac{\mu}{\eta} \text{dev } \boldsymbol{\sigma}^*, \quad (\text{A5})$$

845 where $\boldsymbol{\sigma}^*$ is the manufactured stress and can be obtained by computing

$$846 \quad \boldsymbol{\sigma}^* = \mathbf{E} \underline{\boldsymbol{\varepsilon}}(\mathbf{u}_e). \quad (\text{A6})$$

847 All parameters used are given in Table A1. Table A2 shows the spatial errors $\|\underline{\mathbf{C}} - \underline{\mathbf{C}}_h\|$
 848 and $\|\mathbf{u} - \mathbf{u}_h\|$ when computing approximations to \mathbf{C}^* and \mathbf{u}^* after a single time step, us-
 849 ing a stable step size of 10^{-7} and the discrete L^2 -norm. Successive mesh refinements are

Table A3. Temporal convergence data measured at point $(\tilde{A}, 0)$ under the discrete L^2 -norm.

Δt	$\ \underline{C} - \underline{C}_h\ $	\underline{C} -rate	$\ \mathbf{u} - \mathbf{u}_h\ $	\mathbf{u} -rate
$\Delta t/2$	1.75×10^{-1}		1.18×10^{-6}	
$\Delta t/4$	8.85×10^{-2}	0.99	5.96×10^{-7}	0.99
$\Delta t/8$	4.46×10^{-2}	0.99	3.01×10^{-7}	0.99

850 made using polynomials of degree 3 as a basis for the FEM space. Convergence rates agrees
 851 with FEM theory which predict a convergence rate of $p + 1$ for u^* and p for C^* when
 852 polynomials of degree p are used (Larsson & Thomée, 2008). The same convergence pat-
 853 tern is observed for polynomials with degree greater than 3 except that the L^2 -error drops
 854 below machine precision leading to round-off error in the rate computation.

855 To measure the convergence in the temporal domain we select a single point in space
 856 and perform successive mesh refinements in time. Table A3 shows that both \underline{C} and \mathbf{u}
 857 exhibit rate-1 temporal convergence, consistent with forward Euler.

858 Open Research

859 Software consists of Python code developed on top of the free and open source multi-
 860 physics library NGSolve (Schöberl, 2010–2022) and the accompanying mesh generator (Schöberl,
 861 1997). All source code is freely available in the public repository (*Bitbucket: magmaxisym*,
 862 2022).

863 Acknowledgments

864 CR, BAE and LK were supported by NSF grant EAR- 2036980. LK also acknowl-
 865 edges NSF grant 1848554. BL and JG were supported by NSF grant DMS-1912779. This
 866 work benefited from access to the University of Oregon high performance computer Ta-
 867 lapas and the COEUS cluster at the Portland Institute for Computational Science.

868 References

- 869 Allison, K. L., & Dunham, E. M. (2018). Earthquake cycle simulations with rate-
 870 and-state friction and power-law viscoelasticity. *Tectonophysics*, *733*, 232–256.
 871 doi: <https://doi.org/10.1016/j.tecto.2017.10.021>
- 872 Anderson, K. A., & Segall, P. (2011). Physics-based models of ground deforma-
 873 tion and extrusion rate at effusively erupting volcanoes. *Journal of Geo-*

- 874 *physical Research Solid Earth*, 116(B7), 1–20. doi: [https://doi.org/10.1029/](https://doi.org/10.1029/2010JB007939)
875 2010JB007939
- 876 Bakker, R. R., Frehner, M., & Lupi, M. (2016). How temperature-dependent elas-
877 ticity alters host rock/magmatic reservoir models: A case study on the effects
878 of ice-cap unloading on shallow volcanic systems. *Earth and Planetary Science*
879 *Letters*, 456, 16–25. doi: <https://doi.org/10.1016/j.epsl.2016.09.039>
- 880 Berrino, G., Corrado, G., Luongo, G., & Toro, B. (1984). Ground deformation
881 and gravity changes accompanying the 1982 Pozzuoli uplift. *Bulletin vol-*
882 *canologique*, 47(2), 187–200. doi: <https://doi.org/10.1007/BF01961548>
- 883 *Bitbucket: magmaxisym*. (2022). [https://bitbucket.org/jayggg/magmaxisym/](https://bitbucket.org/jayggg/magmaxisym/src/master/)
884 [src/master/](https://bitbucket.org/jayggg/magmaxisym/src/master/). (Repository with python drivers for computing dynamics of vis-
885 coelastic medium surrounding an axisymmetric magma cavity.)
- 886 Black, B. A., & Manga, M. (2017). Volatiles and the tempo of flood basalt magma-
887 tism. *Earth and Planetary Science Letters*, 458, 130–140. doi: 10.1016/j.epsl
888 .2016.09.035
- 889 Bonafede, M., Dragoni, M., & Quarenì, F. (1986). Displacement and stress fields
890 produced by a centre of dilation and by a pressure source in a viscoelastic half-
891 space: application to the study of ground deformation and seismic activity at
892 Campi Flegrei, Italy. *Geophysical Journal International*, 87(2), 455–485. doi:
893 <https://doi.org/10.1111/j.1365-246X.1986.tb06632.x>
- 894 Bürgmann, R., & Dresen, G. (2008). Rheology of the lower crust and upper mantle:
895 Evidence from rock mechanics, geodesy, and field observations. *Annual Review*
896 *of Earth and Planetary Sciences*, 36, 531–567. doi: [https://doi.org/10.1146/](https://doi.org/10.1146/annurev.earth.36.031207.124326)
897 [annurev.earth.36.031207.124326](https://doi.org/10.1146/annurev.earth.36.031207.124326)
- 898 Carcione, J. M., & Quiroga-Goode, G. (1995). Some aspects of the physics and
899 numerical modeling of biot compressional waves. *Journal of Computational*
900 *Acoustics*, 03(04), 261–280. doi: <https://doi.org/10.1142/S0218396X95000136>
- 901 Chen, A., Erickson, B., & Kozdon, J. (2022). Matrix-free methods for summation-
902 by-parts finite difference operators on GPUs. *submitted*.
- 903 Cianetti, S., Giunchi, C., & Casarotti, E. (2012). Volcanic deformation and flank
904 instability due to magmatic sources and frictional rheology: the case of mount
905 etna. *Geophysical Journal International*, 191, 939–953.
- 906 Currenti, G., & Williams, C. A. (2014). Numerical modeling of deformation and
907 stress fields around a magma chamber: Constraints on failure conditions and
908 rheology. *Physics of the Earth and Planetary Interiors*, 226, 14–27. doi:
909 10.1016/j.pepi.2013.11.003

- 910 Degruyter, W., & Huber, C. (2014). A model for eruption frequency of upper crustal
911 silicic magma chambers. *Earth and Planetary Science Letters*, *403*, 117–130.
912 doi: <https://doi.org/10.1016/j.epsl.2014.06.047>
- 913 Del Negro, C., Currenti, G., & Scandura, D. (2009). Temperature-dependent vis-
914 coelastic modeling of ground deformation: Application to Etna volcano during
915 the 1993–1997 inflation period. *Physics of the Earth and Planetary Interiors*,
916 *172*(3), 299–309. doi: <https://doi.org/10.1016/j.pepi.2008.10.019>
- 917 Dragoni, M., & Magnanensi, C. (1989). Displacement and stress produced
918 by a pressurized, spherical magma chamber, surrounded by a viscoelastic
919 shell. *Physics of the Earth and Planetary Interiors*, *56*(3), 316–328. doi:
920 [10.1016/0031-9201\(89\)90166-0](https://doi.org/10.1016/0031-9201(89)90166-0)
- 921 Erickson, B. A., & Dunham, E. M. (2014). An efficient numerical method for
922 earthquake cycles in heterogeneous media: Alternating subbasin and surface-
923 rupturing events on faults crossing a sedimentary basin. *Journal of Geophysical*
924 *Research: Solid Earth*, *119*(4), 3290–3316. doi: [10.1002/2013JB010614](https://doi.org/10.1002/2013JB010614).
- 925 Erickson, B. A., Dunham, E. M., & Khosravifar, A. (2017). A finite difference
926 method for off-fault plasticity throughout the earthquake cycle. *Journal of the*
927 *Mechanics and Physics of Solids*, *109*, 50–77. doi: [https://doi.org/10.1016/](https://doi.org/10.1016/j.jmps.2017.08.002)
928 [j.jmps.2017.08.002](https://doi.org/10.1016/j.jmps.2017.08.002)
- 929 Golden, J., & Graham, G. (1988). *Boundary value problems in linear viscoelasticity*
930 (1st ed.). Springer-Verlag.
- 931 Gopalakrishnan, J., & Guzmán, J. (2012). A second elasticity element using the ma-
932 trix bubble. *IMA J. Numer. Anal.*, *32*, 352–372. doi: [https://doi.org/10.1093/](https://doi.org/10.1093/imanum/drq047)
933 [imanum/drq047](https://doi.org/10.1093/imanum/drq047)
- 934 Gopalakrishnan, J., & Pasciak, J. E. (2006). The convergence of V-cycle multigrid
935 algorithms for axisymmetric Laplace and Maxwell equations. *Mathematics of*
936 *Computation*, *75*, 1697–1719. doi: [10.1090/S0025-5718-06-01884-9](https://doi.org/10.1090/S0025-5718-06-01884-9)
- 937 Head, M., Hickey, J., Gottsmann, J., & Fournier, N. (2019). The influence of vis-
938 coelastic crustal rheologies on volcanic ground deformation: Insights from
939 models of pressure and volume change. *Journal of Geophysical Research: Solid*
940 *Earth*, *124*(8), 8127–8146. doi: <https://doi.org/10.1029/2019JB017832>
- 941 Head, M., Hickey, J., Gottsmann, J., & Fournier, N. (2021). Exploring the impact of
942 thermally controlled crustal viscosity on volcanic ground deformation. *Journal*
943 *of Geophysical Research: Solid Earth*, *126*(8), e2020JB020724. doi: [10.1029/](https://doi.org/10.1029/2020JB020724)
944 [2020JB020724](https://doi.org/10.1029/2020JB020724)
- 945 Henderson, S. T., & Pritchard, M. E. (2017). Time-dependent deformation of
946 Uturuncu volcano, Bolivia, constrained by GPS and InSAR measurements

- 947 and implications for source models. *Geosphere*, 13(6), 1834–1854. doi:
948 <https://doi.org/10.1130/GES01203.1>
- 949 Huber, C., Townsend, M., Degruyter, W., & Bachmann, O. (2019). Optimal depth
950 of subvolcanic magma chamber growth controlled by volatiles and crust rhe-
951 ology. *Nature Geoscience*, 12(9), 762–768. doi: <https://doi.org/10.1038/s41561-019-0415-6>
- 952
- 953 Jellinek, A. M., & DePaolo, D. J. (2003). A model for the origin of large silicic
954 magma chambers: precursors of caldera-forming eruptions. *Bulletin of Vol-*
955 *canology*, 65(5), 363–381. doi: <https://doi.org/10.1007/s00445-003-0277-y>
- 956 Karakas, O., Degruyter, W., Bachmann, O., & Dufek, J. (2017). Lifetime and size
957 of shallow magma bodies controlled by crustal-scale magmatism. *Nature Geo-*
958 *science*, 10(6), 446–450. doi: <https://doi.org/10.1038/ngeo2959>
- 959 Karlstrom, L., Bacon, C., & Wright, H. (2015). The effect of pressurized magma
960 chamber growth on melt migration and pre-caldera vent locations through
961 time at Mount Mazama, Crater Lake, Oregon. *Earth and Planetary Science*
962 *Letters*, 412, 209–219. doi: 10.1016/j.epsl.2014.12.001
- 963 Karlstrom, L., Dufek, J., & Manga, M. (2010). Magma chamber stability in arc and
964 continental crust. *Journal of Volcanology and Geothermal Research*, 190(3),
965 249–270. doi: 10.1016/j.jvolgeores.2009.10.003
- 966 Karlstrom, L., Paterson, S. R., & Jellinek, A. M. (2017). A reverse energy cascade
967 for crustal magma transport. *Nature Geoscience*, 10(8), 604–608. doi: <https://doi.org/10.1038/ngeo2982>
- 968
- 969 Larsson, S., & Thomée, V. (2008). *Partial differential equations with numerical*
970 *methods* (Vol. 45). Springer Science & Business Media.
- 971 Lau, H. C., & Holtzman, B. K. (2019). “Measures of dissipation in viscoelastic
972 media” extended: Toward continuous characterization across very broad geo-
973 physical time scales. *Geophysical Research Letters*, 46(16), 9544–9553. doi:
974 <https://doi.org/10.1029/2019GL083529>
- 975 Liao, Y., Soule, S. A., Jones, M., & Le Mével, H. (2021). The mechanical response of
976 a magma chamber with poroviscoelastic crystal mush. *Journal of Geophysical*
977 *Research: Solid Earth*, 126(4), e2020JB019395. doi: <https://doi.org/10.1029/2020JB019395>
- 978
- 979 McTigue, D. F. (1987). Elastic stress and deformation near a finite spherical magma
980 body: resolution of the point source paradox. *Journal of Geophysical Re-*
981 *search: Solid Earth*, 92(B12), 12931–12940. doi: <https://doi.org/10.1029/JB092iB12p12931>
- 982

- 983 Mittal, T., & Richards, M. A. (2019). Volatile degassing from magma chambers as
 984 a control on volcanic eruptions. *Journal of Geophysical Research Solid Earth*,
 985 *124*(9), 7869–7901. doi: <https://doi.org/10.1029/2018JB016983>
- 986 Mogi, K. (1958). Relations between the eruptions of various volcanoes and the de-
 987 formations of the ground surfaces around them. *Bulletin of the Earthquake Re-*
 988 *search Institute*, *36*, 99–134.
- 989 Moresi, L., Dufour, F., & Mühlhaus, H.-B. (2002). Mantle convection modeling with
 990 viscoelastic/brittle lithosphere: Numerical methodology and plate tectonic
 991 modeling. *Pure and applied Geophysics*, *159*(10), 2335–2356.
- 992 Muki, R., & Sternberg, E. (1961, 06). On Transient Thermal Stresses in Viscoelas-
 993 tic Materials With Temperature-Dependent Properties. *Journal of Applied Me-*
 994 *chanics*, *28*(2), 193–207. doi: 10.1115/1.3641651
- 995 Newman, A., Dixon, T. H., Ofoegbu, G., & Dixon, J. E. (2001). Geodetic and seis-
 996 mic constraints on recent activity at long valley caldera, california: evidence
 997 for viscoelastic rheology. *Journal of Volcanology and Geothermal Research*,
 998 *105*(3), 183–206. doi: [https://doi.org/10.1016/S0377-0273\(00\)00255-9](https://doi.org/10.1016/S0377-0273(00)00255-9)
- 999 Roache, P. J. (1998). *Verification and validation in computational science and engi-*
 1000 *neering* (Vol. 895). Hermosa Albuquerque, NM.
- 1001 Schetzen, M. (2003). *Linear time-invariant systems* (1st ed.). The Institute of Elec-
 1002 trical and Electronics Engineers.
- 1003 Schöberl, J. (1997). NETGEN an advancing front 2D/3D-mesh generator based on
 1004 abstract rules. *Computing and Visualization in Science*, *1*(1), 41–52. doi: 10
 1005 .1007/S007910050004
- 1006 Schöberl, J. (2010–2022). *NGSolve*. <http://ngsolve.org>.
- 1007 Segall, P. (2010). *Earthquake and volcano deformation*. Princeton University Press.
 1008 doi: 10.1515/9781400833856
- 1009 Segall, P. (2016). Repressurization following eruption from a magma chamber with
 1010 a viscoelastic aureole. *Journal of Geophysical Research: Solid Earth*, *121*(12),
 1011 8501–8522. doi: 10.1002/2016JB013597
- 1012 Segall, P. (2019). Magma chambers: what we can, and cannot, learn from volcano
 1013 geodesy. *Philosophical Transactions of the Royal Society A*, *377*(2139). doi:
 1014 <https://doi.org/10.1098/rsta.2018.0158>
- 1015 Sigmundsson, F., Pinel, V., Lund, B., Albino, F., Pagli, C., Geirsson, H., & Sturkell,
 1016 E. (2010). Climate effects on volcanism: influence on magmatic systems
 1017 of loading and unloading from ice mass variations, with examples from Ice-
 1018 land. *Philosophical Transactions of the Royal Society A*, *368*(1919). doi:
 1019 <https://doi.org/10.1098/rsta.2010.0042>

- 1020 Sparks, R. S. J., Cashman, K., & Calais, E. (2017). Dynamic magma systems:
1021 Implications for forecasting volcanic activity. *Elements*, 13(1), 35–40. doi:
1022 <https://doi.org/10.2113/gselements.13.1.35>
- 1023 Townsend, M. (2022). Linking surface deformation to thermal and mechanical
1024 magma chamber processes. *Earth and Planetary Science Letters*, 577, 117–272.
1025 doi: <https://doi.org/10.1016/j.epsl.2021.117272>
- 1026 Walwer, D., Ghil, M., & Calais, E. (2021). Oscillatory nature of the Okmok vol-
1027 cano’s deformation. *Philosophical Transactions of the Royal Society A*, 506,
1028 76–86. doi: <https://doi.org/10.1016/j.epsl.2018.10.033>